CrossMark

ORIGINAL PAPER

Early Cretaceous (ca. 100 Ma) magmatism in the southern Qiangtang subterrane, central Tibet: Product of slab break-off?

Yalin Li[1] · Haiyang He[1] · Chengshan Wang[1] · Yushuai Wei[1] · Xi Chen[1] · Juan He[2] · Zijie Ning[1] · Aorigele Zhou[1]

Abstract The lack of Early Cretaceous magmatic records with high-quality geochemical data in the southern Qiangtang subterrane has inhibited a complete understanding of the magmatic processes and geological evolution of central Tibet. In this study, we present zircon U–Pb ages, whole-rock geochemistry, and Sr–Nd–Pb and zircon Hf isotopic data for the newly discovered Moku pluton in the southern Qiangtang subterrane. Zircon U–Pb dating reveals that the Moku granites were emplaced in the Early Cretaceous (ca. 100 Ma) and are coeval with the hosted dioritic enclaves. The granites are slightly peraluminous and high-K calc-alkaline I-type granites and characterized by initial $({}^{87}Sr/{}^{86}Sr)_i$ ratios of 0.70605–0.70658, negative $\varepsilon_{Nd}(t)$ values (−4.44 to −3.35), and Nd isotopic model ages of 1.19–1.29 Ga. The granites have a wide range of zircon $\varepsilon_{Hf}(t)$ values (−24.4 to 2.6) and concordant ratios of $({}^{206}Pb/{}^{204}Pb)_t = 18.645–18.711$, $({}^{207}Pb/{}^{204}Pb)_t = 15.656–15.666$, and $({}^{208}Pb/{}^{204}Pb)_t = 38.751–38.836$. The coeval dioritic enclaves are medium- to high-K calc-alkaline rocks with zircon $\varepsilon_{Hf}(t)$ values of −13.3 to +3.6. The geochemical signatures of the host granites and coeval dioritic enclaves indicate that the Moku pluton was most likely generated by partial melting of the ancient lower crust with contributions from mantle-derived melts. Our new data, together with other recently published data, indicate that the ca. 100 Ma magmatic rocks were derived from anatexis of the Qiangtang lower crust that mixed with upwelling asthenosphere materials in response to the slab break-off of the northward subduction of the Bangong–Nujiang oceanic lithosphere.

Keywords Early Cretaceous · Bangong–Nujiang Ocean · Slab break-off · Qiangtang Terrane · Tibet

Introduction

The closure of the Bangong–Nujiang Ocean and the subsequent Lhasa–Qiangtang collision are recognized as the principal events in central Tibet during the Late Jurassic–Early Cretaceous (Girardeau et al. 1984; Dewey et al. 1988; Yin and Harrison 2000; Schneider et al. 2003; Kapp et al. 2005, 2007; Guynn et al. 2006; Li et al. 2015b; Zhu et al. 2016), and their rocks provide an important record for the assembly of the dispersed terranes into Asia and the development of the Tibetan plateau (Yin and Harrison 2000; Li et al. 2015b). Magmatism offers important insights into the subduction of ocean seafloor, continental collision, and mantle–crust interaction in central Tibet (Kapp et al. 2007; Zhang et al. 2012a; Li et al. 2013a, 2015a; Zhu et al. 2016). However, the notable differences in Early Cretaceous magmatism between the northern Lhasa and southern Qiangtang subterranes resulting from the subduction of the Bangong–Nujiang Ocean and subsequent Lhasa–Qiangtang collision remain hotly debated.

The early tectonic models speculated that the Bangong–Nujiang slab was subducted beneath the Qiangtang Terrane together with one or more oceanic island arc terranes (Allègre et al. 1984; Girardeau et al. 1984; Guynn et al. 2006; Kapp et al. 2007). However, the widespread magmatic rocks in the northern Lhasa subterrane and lack

✉ Yalin Li
liyalin@cugb.edu.cn

1 State Key Laboratory of Biogeology and Environmental Geology, School of Earth Sciences and Resources, China University of Geosciences, Beijing 100083, China

2 Chengdu Institute of Geology and Mineral Resources, Chengdu 610082, China

of corresponding magmatism in the southern Qiangtang subterrane led some researchers to suggest that the Bangong–Nujiang Ocean subducted beneath the Lhasa Terrane (Zhu et al. 2009a, 2011, 2013; Pan et al. 2012; Deng et al. 2014) rather than the Qiangtang Terrane (Allègre et al. 1984; Guynn et al. 2006; Kapp et al. 2007; Zhang et al. 2012a; Li et al. 2014a). Moreover, the magmatic flare-up with strong mantle input at ~110 Ma in the northern Lhasa subterrane was attributed to slab break-off of the southward subduction of the Bangong–Nujiang Ocean floor during the Lhasa–Qiangtang collision (Zhu et al. 2009a, 2011; Zhang et al. 2010, 2011, 2012b; Sui et al. 2013). However, the strongly peraluminous to calc-alkaline magmatism and extensional deformation in the Lhasa Terrane were regarded as the results of an orogen that broke down due to lithospheric delamination and asthenospheric upwelling (Zhang et al. 2012a). Moreover, newly discovered magmatic rocks in the southern Qiangtang subterrane confirm that the Bangong–Nujiang Ocean had undergone northward subduction (Li et al. 2014a, b, 2015a, b, 2016b; Geng et al. 2016), which may imply that the Bangong–Nujiang oceanic lithosphere had experienced bidirectional subduction (Zhu et al. 2016). Obviously, the lack of high-quality geochronological and geochemical data in central Tibet inhibits a complete understanding of the subduction polarity of the Bangong–Nujiang oceanic lithosphere and the evolution of central Tibet during the Mesozoic. The previous geodynamic models regarding the subduction of the Bangong–Nujiang oceanic lithosphere should be reappraised, and the Early Cretaceous magmatism in the southern Qiangtang subterrane provides an important window for understanding the evolution of the Bangong–Nujiang Ocean.

In this paper, we report zircon LA–ICPMS age data from the newly discovered granitic rocks of the Moku area in the southern Qiangtang subterrane. We also present whole-rock geochemistry, Sr–Nd–Pb isotopes, and zircon Hf isotopic data to gain a better understanding of the petrogenesis and geodynamics of Early Cretaceous magmatism in the Qiangtang Terrane. Our results indicate that the Moku pluton was emplaced at ca. 100 Ma and most likely resulted from anatexis of the Qiangtang lower crust that mixed with asthenospheric magma in response to the slab break-off of the northward-subducting Bangong–Nujiang oceanic lithosphere. Our results provide valuable constraints on the magmatic processes involved in the subduction of the Bangong–Nujiang Ocean and the Lhasa–Qiangtang collision.

Geological background

The Tibetan plateau is essentially composed of four continental blocks or terranes: the Songpan–Ganzi, Qiangtang, Lhasa, and Himalaya, from north to south (Fig. 1a). These blocks are separated by the Jinsha, Bangong–Nujiang, and Indus–Yarlung Zangbo suture zones, representing Paleo-, Meso-, and Neo-Tethyan oceanic relics, respectively (Yin and Harrison 2000).

The Qiangtang Terrane is located in central Tibet and has a width of 500–600 km (Fig. 1b). The Triassic Shuanghu suture divides the Qiangtang Terrane into northern and southern subterranes (Zhang and Tang 2009). The southern Qiangtang subterrane investigated in this study is dominated by Upper Triassic–Upper Jurassic marine deposits with a thickness of more than 3000 m (Li et al. 2016b), including Middle Jurassic sequences that mainly consist of clastic rocks and Upper Jurassic sequences that are composed of carbonates. These marine deposits are unconformably overlain by weakly deformed Upper Cretaceous continental sediments (i.e., Abushan Formation), which are considered to be the result of the Qiangtang–Lhasa collision (Kapp et al. 2005, 2007; Zhang et al. 2012a; Li et al. 2013a). The subduction-related magmatic rocks previously reported are mainly exposed in the northern Lhasa subterrane, and the lack of corresponding magmatism in the central segment of the southern Qiangtang subterrane is the main reason for disputes regarding the subduction polarity of the Bangong–Nujiang Ocean. The newly discovered Jurassic magmatism in the central segment of the southern Qiangtang subterrane (Li et al. 2015a, 2016b) suggests that the Bangong–Nujiang oceanic lithosphere was subducted northward beneath the Qiangtang Terrane, forming a west–east magmatic arc over more than 800 km long (Li et al. 2016a). Moreover, the recent studies revealed the existence of 96–102 Ma volcanic rocks in the Moku area (Poqu and Madeng) (Fig. 1a, b), which were attributed to the partial melting of relict subducted oceanic crust combined with the input of oceanic sediments (Li et al. 2015a). However, this genetic explanation is primarily based on the geochemical data of major and trace elements, but isotopic data to provide vital constraints on this model are lacking.

The Bangong–Nujiang suture is characterized by a >1400-km-long east–west-trending belt of mainly Jurassic flysch, mélange, and ophiolitic fragments, representing the remnants of the Bangong–Nujiang Ocean (Fig. 1a; Girardeau et al. 1984; Dewey et al. 1988; Schneider et al. 2003; Yin and Harrison 2000; Leier et al. 2007). Although the subduction processes of the Bangong–Nujiang Ocean and geological consequences are still in dispute (Zhu et al. 2009a; Liu et al. 2010; Zhang et al. 2012a), the isotopic ages of the ophiolitic fragments (which range from 190 to 108 Ma) (Zhu et al. 2006b; Zhang et al. 2012a) and the Late Cretaceous terrestrial sediments along this suture indicate that final closure of the Bangong–Nujiang Ocean and the subsequent Lhasa–Qiangtang collision occurred during the Early Cretaceous (Zhang et al. 2012a; Li et al. 2013a; Zhu et al. 2016).

The Lhasa Terrane, which is bounded by the Bangong–Nujiang suture in the north and the Indus–Yarlung suture
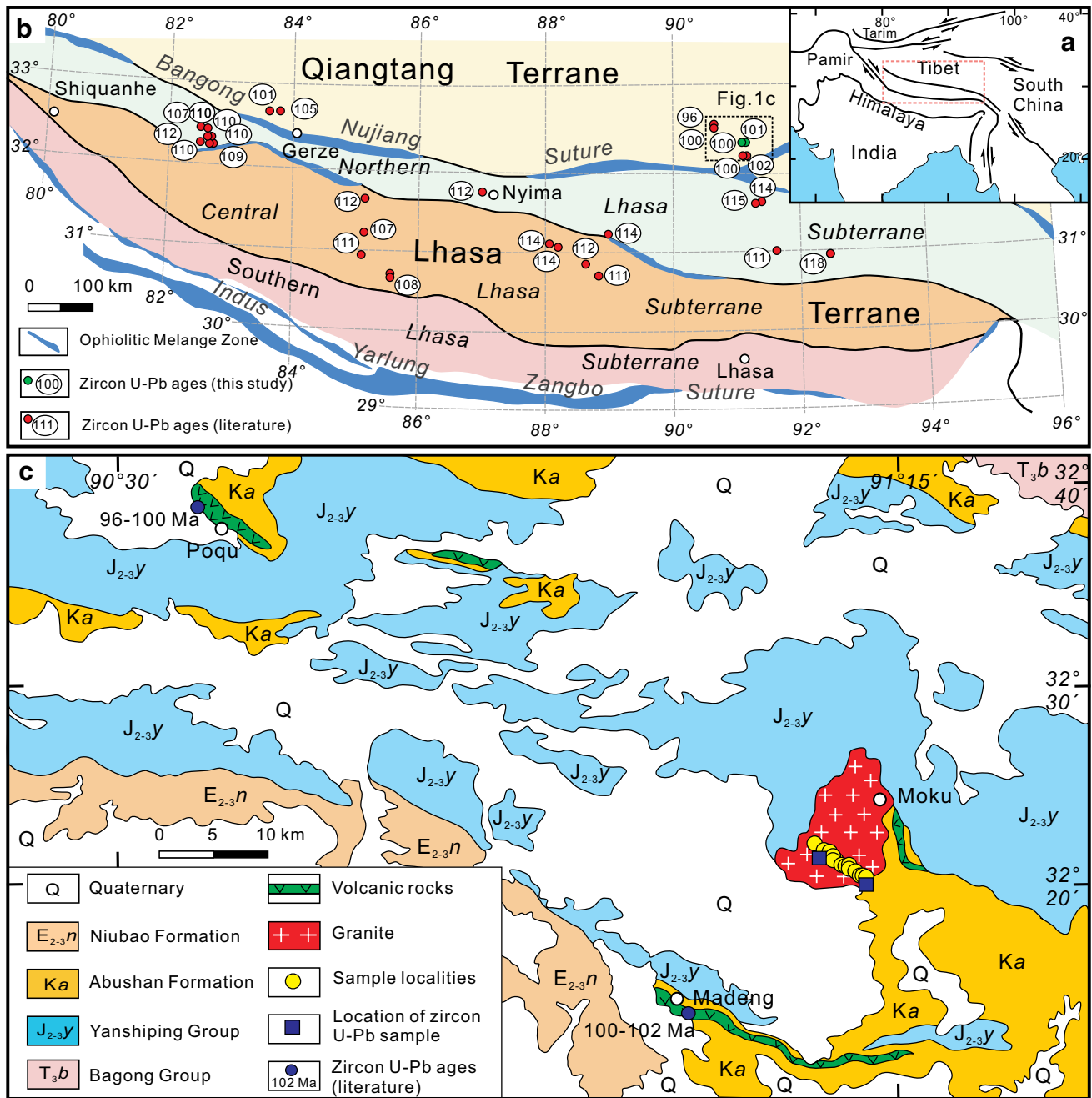
Fig. 1 **a** Tectonic outline of the Tibetan plateau showing major tectonic units. **b** Distribution of the Early Cretaceous magmatic rocks and their ages (ovals with numerals) in northern Lhasa and south-ern Qiangtang subterranes (after Zhu et al. 2009a; Sui et al. 2013; Li et al. 2011, 2015a; Zhang et al. 2010, 2011, 2012b). **c** Geological map of the Moku area

in the south (Fig. 1b), can be divided into northern, central, and southern subterranes. The main rocks exposed in the northern Lhasa subterrane are Jurassic–Early Cretaceous sedimentary and associated magmatic rock (Dewey et al. 1988; Guynn et al. 2006). In contrast with the Qiangtang Terrane, this subterrane contains widespread Cretaceous magmatic rocks (Fig. 1b) (Zhang et al. 2004; Leier et al. 2007; Mo et al. 2007; Zhu et al. 2006a, 2009a, b; 2016).

The arc-related magmatic rocks (>110 Ma) include inter-mediate-silicic intrusions and volcanic rocks and are attrib-uted to the southward subduction of the Bangong–Nujiang oceanic lithosphere beneath the Lhasa subterrane (Zhu et al. 2006a, 2009a, 2011, 2013, 2016; Ma and Yue 2010). The magmatic flare-up with a great compositional diversity (basalt, rhyolite, dioritic enclave, biotite monzogranite, and granite) and the strong input of mantle-derived materials at
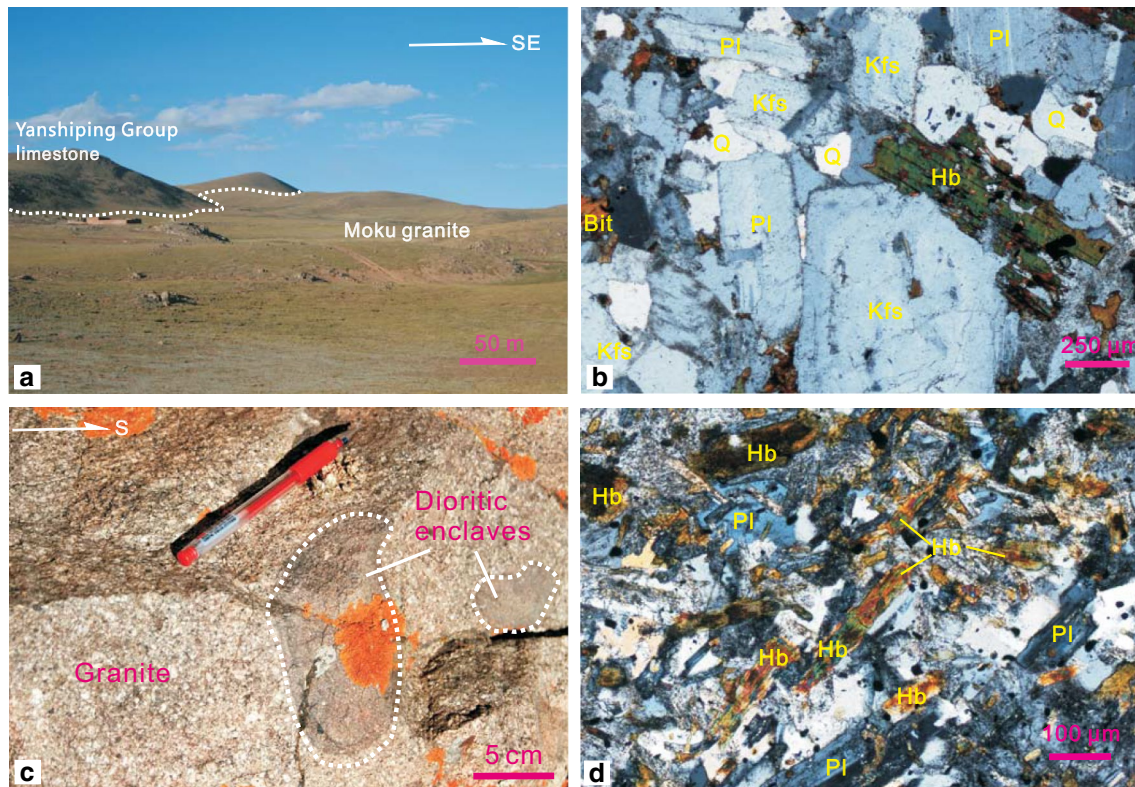
Fig. 2 **a** Field photograph showing the Moku granites pluton into the Jurassic Yanshiping Group. **b** Photomicrographs showing the texture of the host monzogranites. **c** Field photos showing the size of dioritic enclaves and contact with the host monzogranites. **d** Photomi- crographs showing the texture and mineral assemblage of the dioritic enclaves. *Kfs* K-feldspar, *Q* quartz, *Bit* biotite, *Pl* plagioclase, *Hb* hornblende

ca. 110 Ma are interpreted as the results of slab break-off of the southward subducted Bangong–Nujiang oceanic litho- sphere during the Lhasa–Qiangtang collision (Zhu et al. 2006a, 2009a, 2011, 2013, 2016; Ma and Yue 2010; Sui et al. 2013).

Field occurrence and petrography

Samples were collected from the Moku area (E90°14′38″, N32°21′07″) in the southern Qiangtang subterrane adjacent to the Bangong–Nujiang suture (Fig. 1b). The lithostratigraphic units exposed in the Moku area include the Late Triassic Bagong Formation, the Mid- dle–Late Jurassic Yanshiping Group, the Late Cretaceous Abushan Formation, and the Paleogene Niubao Forma- tion (Fig. 1c). With a area of ca. 90 km², the Moku plu- ton intrudes into the Yanshiping Group in the northwest and the Abushan Formation terrestrial sediments in the southeast (Figs. 1c, 2a). Zircon U–Pb data of the volcanic rocks in the lower part of the Abushan Formation indicate that terrestrial sedimentations started at ~100 Ma (Li et al. 2015a).

The Moku pluton is composed primarily of biotite-horn- blende monzogranites (host rocks) with dioritic enclaves. The biotite-hornblende monzogranites are gray and exhibit medium- to coarse-grained igneous texture; they consist of 20–25 % quartz, 30–40 % K-feldspar, 25–30 % plagioclase, 5–10 % hornblende and biotite, as well as minor accessory minerals (Fig. 2b). The dioritic enclaves, with sizes from 5 to 30 cm, are commonly observed within the monzo- granite, generally appear ellipsoidal or lenticular in sec- tion, and have sharp contacts with the host rocks (Fig. 2c). Compared to the host rocks, the dioritic enclaves are fine- grained in texture and consisting of plagioclase (50–55 %), hornblende (30–35 %), quartz (8–10 %), K-feldspar (5 %), biotite (3 %), and minor accessory minerals (Fig. 2d).

Analytical methods

Zircon U–Pb dating

Zircon dating was conducted using LA–ICP–MS methods at the State Key Laboratory for Mineral Deposits Research at Nanjing University using an Agilent 7500a ICP–MS

coupled with a UP213 laser-ablation system (made by New Wave). The analytical procedures used for the U–Pb dating were described in detail by Belousova et al. (2001). The zircon standard 91500 (origin: Ontario, Canada) used for the correction of mass discrimination was analyzed at intervals of 5–7 sample zircon analyses. Afterward, the data from ICP–MS analyses were processed using the GLIT-TER software (Version 4.0). Common Pb was corrected according to Andersen (2002), and the ISOPLOT software (Version 2.49) was used to calculate the weighted zircon ages and produce a concordia plot.

Major and trace elements

All samples were crushed to 200 mesh using an agate mill for major and trace element and Sr–Nd isotopic analyses. Major element oxides (wt%) were determined using a Varian Vista PRO ICP–AES at the Key Laboratory of Isotope Geochronology and Geochemistry, Guangzhou Institute of Geochemistry, Chinese Academy of Sciences (GIGCAS). The details of the analytical procedures were described by Li et al. (2002). Trace elements, including the rare earth elements (REE), were analyzed using a Perkin-Elmer ELAN 6000 inductively coupled plasma source mass spectrometer (ICP–MS) at the GIGCAS, following procedures described by Li et al. (2002).

Whole-rock Sr–Nd–Pb isotopes

The whole-rock Sr, Nd, and Pb isotopic compositions were measured using a Finnigan Triton TI TIMS at the State Key Laboratory for Mineral Deposits Research, Nanjing University. The detailed separation procedures and mass spectrometry analyses were the same as those described by Pu et al. (2005). The mass fractionation corrections for $^{87}Sr/^{86}Sr$ and $^{143}Nd/^{144}Nd$ ratios were based on $^{86}Sr/^{88}Sr = 0.1194$ and $^{146}Nd/^{144}Nd = 0.7219$, respectively. Repeated analyses of the JNdi–1 Nd standard yielded a $^{143}Nd/^{144}Nd$ ratio of 0.512121 ± 0.000016 (2σ, $n = 5$), and the NBS-987 Sr standard yielded $^{87}Sr/^{86}Sr = 0.710260 \pm 0.000010$ (2σ, $n = 30$). Total analytical blanks were 5×10^{-11} g for Sm and Nd and $(2–5) \times 10^{-10}$ g for Rb and Sr.

For Pb isotope determination, approximately 50 mg of the feldspar samples was completely dissolved in an ultrapure $HNO_3 + HCl$ mixture. After drying, the residue was dissolved in an $HBr + HNO_3$ mixture and then loaded into a column with 50 Am of AG 1-X 8 anionic resins. The extracted Pb was then purified in a second column. Approximately, 100 ng of Pb was loaded onto a single rhenium filament using the silica gel technique. Analytical reproducibilities of 0.01 % (2σ) for $^{206}Pb/^{204}Pb$, 0.01 % for $^{207}Pb/^{204}Pb$, and 0.02 % for $^{208}Pb/^{204}Pb$ were attained in this study. Mass fractionation corrections were made from

runs of the NBS-981 standard based on the suggested value of Todt et al. (1996), and the error of the mass fractionation corrections was 0.04 %.

Zircon Hf isotopic analysis

In situ zircon Lu–Hf isotopic measurements were performed on a Neptune multi-collector ICP–MS equipped with a Geolas-193 laser-ablation system with a laser pulse frequency of 8 Hz at the Institute of Geology and Geophysics, Chinese Academy of Sciences, Beijing. Instrumental conditions and data acquisition were similar to those described by Wu et al. (2006). Measured $^{176}Hf/^{177}Hf$ ratios were normalized to $^{179}Hf/^{177}Hf = 0.7325$. The $\varepsilon_{Hf}(t)$ values and TDM were calculated following Griffin et al. (2000) using the ^{176}Lu decay constant given in Blichert-Toft and Albarède (1997).

Geochronology and geochemistry results

Zircon U–Pb geochronology

Three samples were selected for dating, including two samples from the host granites (UKG and HKV) and one sample (BT-9) from a dioritic enclave (Fig. 1b). The zircon U–Pb analytical data and calculation results are listed in Table 1.

Zircons from the two host granites show euhedral morphology and are mainly long and prismatic with long axes of 200–400 μm and length/width ratios of 2:1–6:1. Cathodoluminescence (CL) images reveal that the zircon crystals possess clear oscillatory zoning and lack any inherited cores (Fig. 3a, b). These, together with the high Th/U ratios (0.30–0.70) of the dated analyses, suggest an origin by crystallization from magmas. Nineteen zircons from UKG yield $^{206}Pb/^{238}U$ ages ranging from 98 ± 0.8 to 102 ± 0.9 Ma, with a weighted mean age of 100.3 ± 0.6 Ma (MSWD = 1.9, $n = 19$) (Fig. 3d). Twenty zircons from HKV yield $^{206}Pb/^{238}U$ ages between 100 ± 1.0 and 102 ± 0.9 Ma, with a weighted mean age of 100.6 ± 0.5 Ma (MSWD = 0.6, $n = 20$) (Fig. 3e). These data suggest that the Moku pluton was emplaced during the Early Cretaceous (ca. 100 Ma).

Except for their smaller size, zircons from the dioritic enclave (BT-9) exhibit morphology, crystal structure, and Th/U ratios (0.30–0.90) similar to zircons from the host granites (Fig. 3c). Seventeen zircons yield $^{206}Pb/^{238}U$ ages ranging from 100 ± 2.0 to 101 ± 2.0 Ma, with a weighted mean age of 100.3 ± 0.8 Ma (MSWD = 0.1, $n = 17$) (Fig. 3f). The zircon U–Pb dating results indicate that the Moku granites are coeval with their dioritic enclaves and areal volcanic rocks in Madeng and Poqu (Li et al. 2015a).

Table 1 Zircon age data acquired by LA-ICPMS methods for the Moku granites and dioritic enclaves

Samples and Anal. No.	Th (ppm)	U (ppm)	Th/U Ratio	Isotopic ratios (±1σ)						Ages (±1σ Ma)					
				$^{207}Pb/^{206}Pb$	±1σ	$^{207}Pb/^{235}U$	±1σ	$^{206}Pb/^{238}U$	±1σ	$^{207}Pb/^{206}Pb$	±1σ	$^{207}Pb/^{235}U$	±1σ	$^{206}Pb/^{238}U$	±1σ
Sample UKG															
1. UKG-01	383.3	1120.3	0.3	0.05177	0.00091	0.11251	0.00178	0.01577	0.00012	275	41	108	2	101	0.8
2. UKG-05	420.2	964.4	0.4	0.04942	0.00107	0.10721	0.00216	0.01574	0.00013	168	52	103	2	101	0.8
3. UKG-06	488.1	879.8	0.6	0.05183	0.00141	0.1135	0.00291	0.01589	0.00014	278	64	109	3	102	0.9
4. UKG-07	451.3	993.2	0.5	0.04883	0.00135	0.10526	0.00276	0.01564	0.00014	140	66	102	3	100	0.9
5. UKG-09	343.5	810.1	0.4	0.04972	0.00098	0.10502	0.0019	0.01532	0.00012	182	47	101	2	98	0.8
6. UKG-10	530.4	1041.5	0.5	0.04981	0.00134	0.10622	0.0027	0.01547	0.00014	186	64	103	2	99	0.9
7. UKG-11	170.0	424.6	0.4	0.04883	0.00159	0.10558	0.0033	0.01569	0.00015	140	77	102	3	100	1.0
8. UKG-14	508.4	841.3	0.6	0.05125	0.00185	0.10953	0.00381	0.0155	0.00015	252	85	106	3	99	1.0
9. UKG-15	382.0	843.4	0.5	0.05067	0.00114	0.1098	0.00229	0.01572	0.00013	226	53	106	2	101	0.8
10. UKG-17	513.5	978.7	0.5	0.04989	0.00165	0.10727	0.0034	0.0156	0.00015	190	79	103	3	100	1.0
11. UKG-18	571.1	1095.1	0.5	0.05326	0.00094	0.11651	0.00186	0.01587	0.00012	340	41	112	2	102	0.8
12. UKG-19	560.1	1223.6	0.5	0.05009	0.00092	0.10948	0.00181	0.01585	0.00012	199	44	105	2	101	0.8
13. UKG-20	330.3	698.8	0.5	0.04841	0.00125	0.10598	0.00257	0.01588	0.00014	119	62	102	2	102	0.9
14. UKG-21	370.4	864.5	0.4	0.04812	0.00101	0.1032	0.00199	0.01556	0.00012	105	51	100	2	100	0.8
15. UKG-22	602.0	1209.5	0.5	0.05211	0.0019	0.11158	0.00392	0.01553	0.00016	290	85	107	4	99	1.0
16. UKG-23	339.2	883.1	0.4	0.04974	0.00157	0.10718	0.00323	0.01563	0.00015	183	75	103	3	100	1.0
17. UKG-24	269.4	656.6	0.4	0.04961	0.0011	0.10782	0.00223	0.01577	0.00013	177	53	104	2	101	0.8
18. UKG-25	443.8	1132.4	0.4	0.04775	0.00104	0.10108	0.00204	0.01535	0.00012	87	52	98	2	98	0.8
19. UKG-026	362.9	1037.2	0.3	0.04843	0.00102	0.10581	0.00206	0.01585	0.00013	120	51	102	2	101	0.8
Sample HKV															
1. HKV-02	229.6	881.3	0.3	0.0489	0.00154	0.10602	0.00317	0.01573	0.00015	143	75	102	3	101	1.0
2. HKV-03	371.0	939.0	0.4	0.05333	0.00163	0.11508	0.00333	0.01565	0.00015	343	71	111	3	100	1.0
3. HKV-04	571.8	1260.3	0.5	0.04749	0.00101	0.10322	0.00203	0.01576	0.00013	74	50	100	2	101	0.8
4. HKV-05	319.0	743.8	0.4	0.05291	0.00237	0.11484	0.00496	0.01575	0.00019	325	104	110	5	101	1.0
5. HKV-06	433.7	1086.4	0.4	0.04701	0.00122	0.10141	0.00248	0.01565	0.00013	50	57	98	2	100	0.8
6. HKV-07	372.1	1053.9	0.4	0.049	0.00096	0.10671	0.0019	0.0158	0.00012	148	47	103	2	101	0.8
7. HKV-08	236.0	649.1	0.4	0.04809	0.00133	0.10422	0.00274	0.01572	0.00014	104	65	101	3	101	0.9
8. HKV-10	368.5	959.4	0.4	0.04875	0.00109	0.10658	0.00221	0.01586	0.00013	136	54	103	2	101	0.8
9. HKV-11	317.9	642.9	0.5	0.05197	0.00132	0.11347	0.0027	0.01584	0.00014	284	59	109	2	101	0.9
10. HKV-13	358.0	530.5	0.7	0.0511	0.00255	0.11115	0.00542	0.01578	0.00017	245	117	107	5	101	1.0
11. HKV-15	384.4	960.5	0.4	0.05062	0.00142	0.10923	0.00289	0.01565	0.00014	224	66	105	3	100	0.9
12. HKV-17	464.3	1481.1	0.3	0.04903	0.00105	0.10535	0.00211	0.01558	0.00012	149	52	102	2	100	0.8
13. HKV-19	499.0	1169.2	0.4	0.04861	0.00116	0.10552	0.00235	0.01575	0.00013	129	57	102	2	101	0.8

Table 1 continued

| Samples and Anal. No.	Th (ppm)	U (ppm)	Th/U Ratio	Isotopic ratios (±1σ)						Ages (±1σ Ma)					
				$^{207}Pb/^{206}Pb$		$^{207}Pb/^{235}U$		$^{206}Pb/^{238}U$		$^{207}Pb/^{206}Pb$		$^{207}Pb/^{235}U$		$^{206}Pb/^{238}U$	
14. HKV-20	401.1	970.3	0.4	0.0483	0.00143	0.10415	0.00292	0.01564	0.00014	114	70	101	3	100	0.9
15. HKV-21	391.3	776.1	0.5	0.05207	0.00187	0.11396	0.00392	0.01587	0.00016	289	84	110	4	102	1.0
16. HKV-022	240.6	593.4	0.4	0.05069	0.00138	0.11102	0.00286	0.01589	0.00014	227	64	107	3	102	0.9
17. HKV-023	314.8	899.6	0.3	0.04971	0.00147	0.10756	0.00303	0.01569	0.00014	181	70	104	3	100	0.9
8. HKV-024	688.1	1422.4	0.5	0.05005	0.00083	0.10972	0.0016	0.0159	0.00012	197	39	106	1	102	0.8
19. HKV-025	317.8	803.7	0.4	0.04972	0.00109	0.1088	0.00222	0.01588	0.00013	182	52	105	2	102	0.8
20. HKV-026	483.8	1296.3	0.4	0.04724	0.00093	0.102	0.00183	0.01566	0.00012	61	46	99	2	100	0.8
Sample BT-9															
1. BT-9-12	953.0	1968.2	0.5	0.04412	0.00221	0.09549	0.00484	0.01569	0.00026	-64	108	93	4	100	2.0
2. BT-9-14	701.0	2587.1	0.3	0.05258	0.00204	0.11424	0.00475	0.01571	0.00025	311	91	110	4	100	2.0
3. BT-9-15	916.4	2441.3	0.4	0.05000	0.00209	0.10782	0.00463	0.01565	0.00024	195	99	104	4	100	1.0
4. BT-9-19	1377.4	2966.7	0.5	0.05118	0.00254	0.11179	0.00690	0.01569	0.00034	249	117	108	6	100	2.0
5. BT-9-21	863.8	1971.7	0.4	0.05153	0.00218	0.11158	0.00474	0.01571	0.00024	264	100	107	4	101	2.0
6. BT-9-23	866.9	2358.9	0.4	0.04628	0.00191	0.10022	0.00427	0.01570	0.00028	12	88	97	4	100	2.0
7. BT-9-25	1753.5	2047.4	0.9	0.04820	0.00195	0.10417	0.00433	0.01569	0.00025	109	92	101	4	100	2.0
8. BT-9-26	1142.0	2556.4	0.4	0.05056	0.00182	0.10906	0.00417	0.01563	0.00028	221	85	105	4	100	2.0
9. BT-9-29	806.2	1931.1	0.4	0.04854	0.00228	0.10500	0.00486	0.01572	0.00023	126	107	101	4	101	1.0
10. BT-9-30	699.7	1082.5	0.6	0.04405	0.00227	0.09449	0.00485	0.01577	0.00026	-68	112	92	4	101	2.0
11. BT-9-35	466.9	904.2	0.5	0.04782	0.00314	0.10186	0.00643	0.01568	0.00029	91	147	98	6	100	2.0
12. BT-9-36	1051.1	2189.3	0.5	0.04652	0.00236	0.10025	0.00487	0.01573	0.00025	25	110	97	4	101	2.0
13. BT-9-38	251.7	359.4	0.7	0.04523	0.00405	0.09763	0.00783	0.01570	0.00040	-8	185	95	7	100	2.0
14. BT-9-39	909.7	2273.4	0.4	0.04647	0.00147	0.10069	0.00348	0.01568	0.00026	22	67	97	3	100	2.0
15. BT-9-41	943.2	2126.9	0.4	0.04874	0.00226	0.10456	0.00497	0.01569	0.00027	135	106	101	5	100	2.0
16. BT-9-42	682.3	1534.2	0.4	0.05086	0.00231	0.11024	0.00514	0.01568	0.00024	234	107	106	5	100	2.0
17. BT-9-43	373.0	695.0	0.5	0.05243	0.00379	0.10992	0.00715	0.01559	0.00037	304	167	106	7	100	2.0
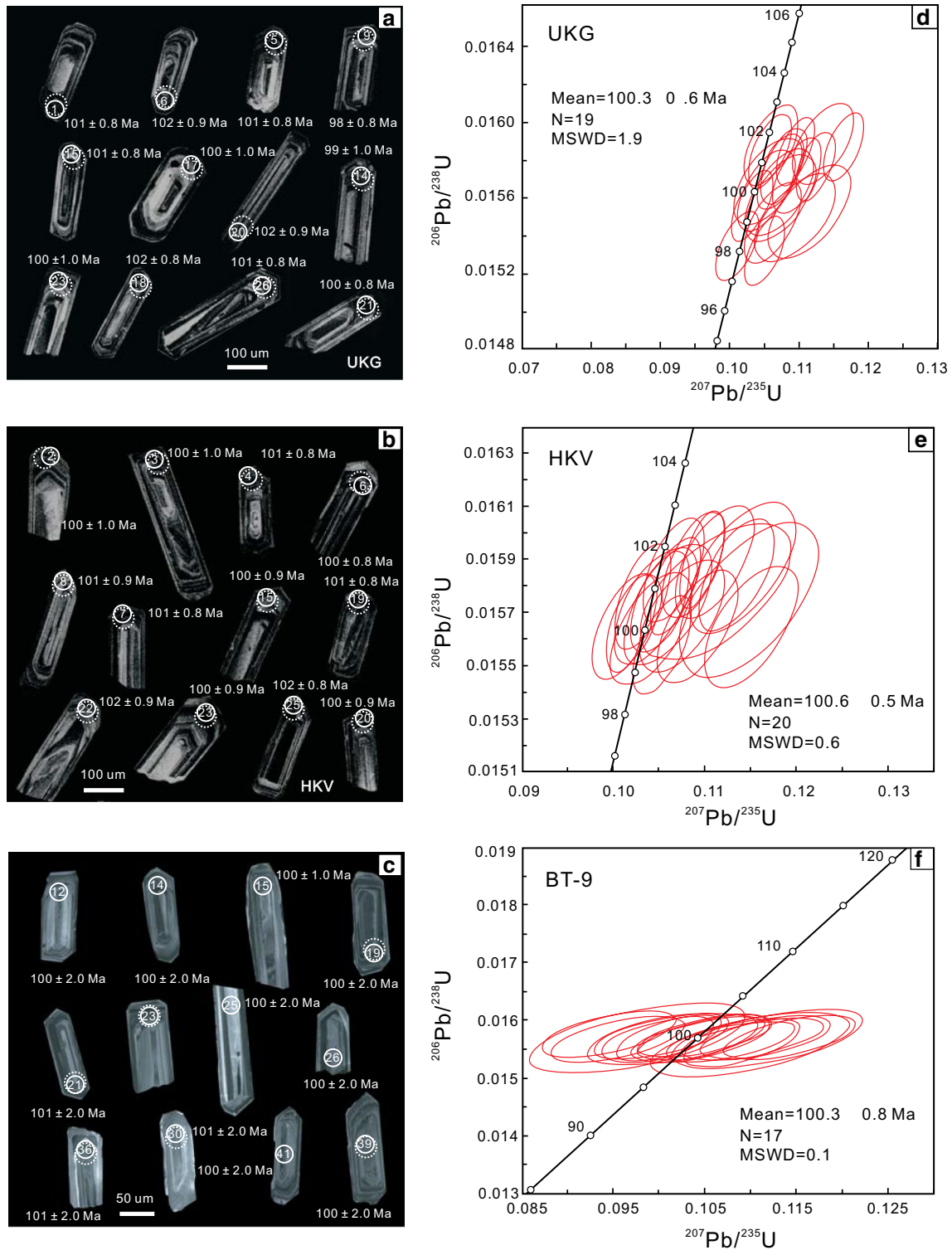
Fig. 3 Cathodoluminescence (CL) images (**a**–**c**) and concordia diagrams (**d**–**f**) for zircons from the host monzogranites (UKG and HKV) and dioritic enclave (BT-9). *Solid* and *dashed circles* indicate the locations of LA-ICPMS U–Pb analyses and Hf isotope analyses, respectively

Whole-rock geochemistry

Fifteen host monzogranite samples and seven enclave samples were selected for whole-rock major and trace element analyses (Fig. 1c). The analytical results are listed in Table 2. The host monzogranites show high SiO_2 (65.40−68.33 wt%), K_2O (3.43-3.89 wt%), Na_2O (3.51–4.11 wt%) and total alkalis ($K_2O + Na_2O$ = 7.17–8.08 wt%), and they plot in the granite field (Fig. 4a). In the K_2O–SiO_2 diagram, all of the samples lie in the field of high-K calc-alkaline rocks and are similar to the ca. 110 Ma magmatic rocks in the northern Lhasa subterrane (Fig. 4b). The host monzogranites have low MgO (1.12–1.45 wt%), Fe_2O_3 (3.74–4.34 wt%), and CaO (1.89–2.80 wt%). The high-K calc-alkaline and peraluminous (A/CNK = 1.01–1.08) (Fig. 4c) characteristics indicate that they are I-type granites (Chappell and White 1992). In contrast, the dioritic enclaves plot in the fields of diorite and quartz diorite (Fig. 4a). They are calc-alkaline to high-K calc-alkaline (Fig. 4b) and metaluminous, with A/CNK ranging from 0.92 to 0.97 (except for one value of 1.05, in sample AD–2) (Fig. 4c). In addition, the dioritic enclaves have lower SiO_2 (58.57−63.96 wt%) and K_2O (1.88–2.94 wt%) and higher Fe_2O_3 (5.00–9.36 wt%), CaO (2.40–4.62 wt%), MgO (2.27–3.56 wt%), and $Mg^\#$ [$Mg^\# = 100 \times Mg^{2+}/(Mg^{2+}+TFe^{2+})$] (43.20–50.90) than the host monzogranites.

The samples from the host monzogranites and dioritic enclaves have similar rare earth elements (REE) characteristics. In the chondrite-normalized REE diagram, both of the rock types (except for sample AD-2) display evident fractionation between light rare earth elements (LREE) and heavy rare earth elements (HREE) and negative to positive Eu anomalies (Fig. 5a; Table 2). In primitive-mantle-normalized spider diagrams (Fig. 5b), the host monzogranites and the dioritic enclaves show coherent patterns, with high light rare earth elements (LREE, such as Rb, Pb, Th) and low depletion in high field strength elements (HFSE, such as Nb, Ta, Ti). These geochemical signatures are consistent with those of the ca. 110 Ma magmatic rocks in the northern Lhasa subterrane and the Poqu volcanic rocks (Fig. 5b).

Fifteen host monzogranite samples were used for whole-rock Sr–Nd–Pb isotope analyses, and the results are listed in Table 2. All of the samples show homogeneous Sr–Nd–Pb isotopic compositions. They show $(^{87}Sr/^{86}Sr)_i$ ranging from 0.70605 to 0.70658, with $\varepsilon_{Nd}(t)$ from −4.44 to −3.35 (Table 2) and Nd model ages ranging from 1.19 to 1.29 Ga. In the $\varepsilon_{Nd}(t)$–$(^{87}Sr/^{86}Sr)_i$ diagram, all of the samples plot along the mixing line between the Bangong–Nujiang ophiolites and the lower crustal mafic granulitic xenoliths of the Qiangtang Terrane (Fig. 6). The initial Pb isotopic ratios of the host monzogranite are uniform: $(^{206}Pb/^{204}Pb)t$ = 18.645–18.711;

$(^{207}Pb/^{204}Pb)t$ = 15.656–15.666; $(^{208}Pb/^{204}Pb)t$ = 38.751–38.836. On plots of $^{207}Pb/^{204}Pb$ and $^{208}Pb/^{204}Pb$ versus $^{206}Pb/^{204}Pb$ (Fig. 7), all of the samples fall significantly above the Northern Hemisphere Reference Line (NHRL) and are distributed in the field between DM and EMΠ.

Zircon Hf isotopes

Two host monzogranite samples (UKG and HKV) and one dioritic enclave sample (BT-9) were analyzed for in situ Hf isotope analyses on the same or similar sites as U–Pb dating (Fig. 3a–c). The analytical results are listed in Table 3. Except for three zircons (UKG–11, 21, 23, with $^{176}Lu/^{177}Hf$ values form 0.002122 to 0.002463), most zircons have $^{176}Lu/^{177}Hf$ ratios less than 0.002, indicating a negligible amount of radiogenic ^{177}Hf. Thirty-six zircons from the two host monzogranites show $^{176}Lu/^{177}Hf$ ratios ranging from 0.000859 to 0.001902 and $^{176}Hf/^{177}Hf$ varying from 0.282021 to 0.282787. The corresponding $\varepsilon_{Hf}(t)$ values are from −24.4 to 2.6 (UKG: −13.8 to +2.6; HKV: −24.4 to +2.2), and the two-stage Hf model ages (T_{DM}^C) range from 0.93–2.50 Ga, clustering at ~1.10 Ga. The dioritic enclave exhibits $^{176}Lu/^{177}Hf$ ratios varying from 0.000543 to 0.002186 and $^{176}Hf/^{177}Hf$ ratios ranging from 0.282339 to 0.282814. The $\varepsilon_{Hf}(t)$ values are from −13.3 to +3.6, and T_{DM}^C ranges from 0.87 to 1.85 Ga.

Discussion

Genetic types of granites

Granite petrogenesis and geodynamic mechanisms are closely related to genetic types. The Moku granites have relatively low SiO_2 contents (65.40–68.33 wt%) and A/CNK values (1.01–1.08) and high K_2O contents (3.43–3.89 wt%), and they are free of typical peraluminous minerals (e.g., cordierite, muscovite, and garnet). All of these characteristics are identical to those of typical I-type granites in the Lachlan Fold Belt (Chappell and White 1992), suggesting that the Moku granites are high-K calc-alkaline I-type granites. P_2O_5 concentrations in I-type granites decrease with increasing SiO_2; in contrast, P_2O_5 in S-type granites is either roughly constant or slightly increases with increasing SiO_2 concentrations (Chappell 1999; Wu et al. 2003; Li et al. 2007). The P_2O_5 contents of the Moku granites decrease markedly with increasing SiO_2 contents (Fig. 8a), consistent with the evolutionary tendency of I-type granites. In addition, all of the Moku host rocks and dioritic enclaves fall in the I-type granite field in the K_2O versus Na_2O diagram (Fig. 8b). In summary, both petrological and geochemical features denote clearly that the Moku granites have the characteristics of I-type granites.

Table 2 Bulk-rock major, trace element and Sr–Nd–Pb isotopic data of the Moku granites

Sample	Granite															Dioritic enclave						
Rock-type	HKV-01	HKV-02	HKV-03	HKV-04	HKV-05	HKV-06	HKV-07	HKV-08	HKV-03	HKV-05	HKV-06	HKV-10	HKV-11	HKV-12	HKV-15	AD-1	AD-2	AD-2	AD-4	AD-5	AD-6	AD-7
Major element (wt%)																						
SiO$_2$	68.33	67.82	66.94	67.48	67.39	67.38	67.23	67.87	65.4	67.87	67.27	67.21	67.45	67.64	67.13	63.01	58.57	63.54	63.13	60.67	60.38	63.96
TiO$_2$	0.56	0.54	0.60	0.58	0.59	0.63	0.60	0.63	0.60	0.60	0.66	0.64	0.62	0.64	0.63	0.821	0.896	0.761	0.811	0.824	1.05	0.777
Al$_2$O$_3$	15.02	15.18	15.08	15.26	15.29	15.18	15.44	15.02	14.85	15.08	14.98	15.36	15.23	15.07	15.16	15.64	14.98	15.84	15.75	15.75	16.05	15.2
Fe$_2$O$_3$	3.78	3.74	4.01	3.94	4.06	4.21	4.01	4.04	3.92	4.06	4.34	4.12	4.17	4.15	4.08	5.42	9.36	5.16	5.28	5.48	6.39	5.00
MnO	0.06	0.07	0.06	0.07	0.07	0.07	0.06	0.06	0.07	0.06	0.06	0.07	0.06	0.07	0.06	0.08	0.13	0.07	0.08	0.13	0.11	0.08
MgO	1.14	1.12	1.27	1.36	1.25	1.36	1.25	1.21	1.27	1.35	1.45	1.28	1.32	1.31	1.4	2.54	3.56	2.47	2.48	2.84	2.98	2.27
CaO	1.89	2.04	2.26	2.3	2.57	2.5	2.61	2.53	2.59	2.79	2.67	2.54	2.8	2.58	2.32	4.17	2.4	4.22	4.33	4.1	4.62	3.45
Na$_2$O	3.78	4.11	3.84	3.75	3.85	3.74	3.8	3.64	3.63	3.52	3.51	3.72	3.64	3.54	3.98	3.96	4.2	4.01	4.05	3.92	4.01	4.08
K$_2$O	3.89	3.86	3.64	3.68	3.46	3.59	3.63	3.75	3.43	3.69	3.57	3.59	3.66	3.67	3.7	2.2	2.76	1.96	2.15	2.94	1.88	2.93
P$_2$O$_5$	0.15	0.14	0.16	0.15	0.15	0.17	0.15	0.16	0.20	0.17	0.17	0.16	0.15	0.16	0.16	0.19	0.20	0.18	0.19	0.18	0.28	0.20
L.O.I	1.43	1.44	2.13	1.42	1.31	1.14	1.21	1.09	4.02	0.78	1.24	1.28	0.84	1.13	1.37	1.87	2.86	1.69	1.71	3.06	2.13	1.93
Total	100.03	100.05	99.99	100.00	99.98	99.96	100.00	100.00	99.99	99.96	99.92	99.97	99.94	99.95	99.99	99.90	99.91	99.90	99.96	99.89	99.88	99.88
A/CNK	1.08	1.04	1.05	1.06	1.04	1.04	1.03	1.03	1.03	1.01	1.03	1.05	1.01	1.04	1.03	0.95	1.05	0.97	0.93	0.92	0.94	0.94
K$_2$O + Na$_2$O	7.78	8.08	7.64	7.54	7.41	7.42	7.52	7.47	7.36	7.27	7.17	7.40	7.36	7.30	7.79	6.28	7.17	6.08	6.31	7.08	6.03	7.16
Mg#	37.62	37.46	38.78	40.84	38.11	39.25	38.40	37.46	39.32	39.94	40.06	38.32	38.77	38.70	40.70	48.38	43.20	48.91	48.44	50.90	48.26	47.59
Na$_2$O/K$_2$O	0.97	1.06	1.05	1.02	1.11	1.04	1.05	0.97	1.06	0.95	0.98	1.04	0.99	0.96	1.08	1.80	1.52	2.05	1.88	1.33	2.13	1.39
Trace element (ppm)																						
Sc	9.22	9.22	8.76	9.84	10.28	10.04	9.80	10.26	9.83	10.08	10.67	10.14	10.27	10.02	10.04	15.1	18.6	14.7	14.1	14.5	17.4	14.3
V	32.7	33.6	26.5	36.8	43.1	39.4	37.9	39.3	35.1	39.3	40.9	39.9	40.7	37.1	39.0	69.9	86.3	73.2	67.9	68.0	99.2	69.7
Cr	9.2	9.1	10.8	13.1	14.6	10.8	12.8	14.3	13.8	14.6	14.0	14.7	17.5	17.3	13.6	14.2	74.5	16.4	12.6	12.4	22.9	23.1
Co	5.0	4.9	4.2	5.3	6.7	6.1	5.8	6.0	5.3	6.2	6.4	6.2	6.4	5.9	5.99	13.4	19.4	13.5	12.5	13	13.7	10.1
Ni	3.9	2.9	4.4	5.4	5.4	2.9	4.7	4.4	4.1	3.4	3.2	3.7	4.4	6.2	3.9	6.1	9.7	5.5	4.3	3.9	4.0	7.0
Ga	19.1	20.1	18.2	20.1	21.6	19.7	19.2	19.3	17.4	19.7	18.4	19.6	19.5	18.2	18.8	19.0	21.7	19.3	18.4	16.6	19.4	18.6
Rb	167.6	173.5	159.1	171.3	155.8	154.8	153.8	162.0	144.3	166.3	154.0	153.5	160.4	152.8	163.5	105.0	157.0	97.7	101.0	117.0	86.3	108.0
Sr	251	239	230	289	280	266	280	265	271	261	255	277	269	258	276	272	215	278	277	252	303	287
Y	32.8	33.7	32.0	32.9	32.0	34.0	31.1	32.6	30.9	33.4	33.5	28.8	33.8	31.3	30.9	29.5	57.8	29.3	27.4	25.7	29.9	32.2
Zr	279	271	235	289	278	274	259	279	243	277	269	67	275	257	279	191	197	218	194	196	185	182
Nb	20.1	20.4	17.7	21.4	21.3	21.2	19.7	21.0	17.2	21.4	19.6	20.5	20.7	19.5	20.3	15.8	19.2	14.8	15.6	14.0	17.1	20.8
Ba	745	756	718	728	666	737	765	751	719	711	731	752	688	720	691	361	353	323	347	438	264	600
La	43.0	50.0	47.9	45.8	44.2	46.6	43.8	43.8	43.9	44.6	44.0	43.7	44.5	43.8	44.0	37.3	30.6	38.7	37.7	35.5	35.3	41.9
Ce	87.4	100.9	95.6	92.8	89.5	93.9	89.9	89.3	87.2	91.1	85.4	85.8	88.7	87.3	89.6	70.4	68.3	66.6	69.2	63.3	65.4	75.8
Pr	9.66	10.93	10.48	10.14	9.92	10.37	9.76	9.82	9.74	9.91	9.89	9.74	9.91	9.66	9.63	8.31	9.46	7.64	7.75	7.25	7.97	9.11
Nd	35.8	40.1	38.3	37.6	36.9	38.3	36.1	36.5	36.1	36.8	37.0	36.1	36.9	35.7	35.4	33.3	43.7	30.4	30.5	28.2	33.3	35.4
Sm	7.09	7.65	7.33	7.35	7.41	7.55	7.13	7.28	7.04	7.30	7.38	7.07	7.33	7.02	6.84	6.05	10.70	6.10	5.93	5.45	6.14	7.12
Eu	1.12	1.25	1.19	1.25	1.25	1.23	1.26	1.21	1.24	1.21	1.19	1.26	1.20	1.17	1.22	1.26	0.86	1.30	1.46	1.26	1.20	1.29
Gd	6.59	6.97	6.68	6.80	6.79	6.99	6.49	6.71	6.46	6.76	6.85	6.43	6.82	6.46	6.32	5.31	9.49	5.37	5.03	4.73	5.56	5.76

Table 2 continued

Sample	Granite															Dioritic enclave						
Rock-type	HKV-01	HKV-02	HKV-03	HKV-04	HKV-05	HKV-06	HKV-07	HKV-08	HKV-03	HKV-05	HKV-06	HKV-10	HKV-11	HKV-12	HKV-15	AD-1	AD-2	AD-2	AD-4	AD-5	AD-6	AD-7
Tb	0.97	1.01	0.97	0.99	1.01	1.02	0.95	0.99	0.93	1.00	1.00	0.93	1.00	0.94	0.91	1.00	1.95	0.93	0.88	0.89	1.00	1.10
Dy	5.81	5.99	5.72	5.83	5.96	6.04	5.62	5.89	5.54	5.93	5.93	5.46	5.98	5.56	5.40	5.48	10.60	5.26	5.06	4.99	5.46	5.90
Ho	1.13	1.17	1.12	1.14	1.16	1.18	1.09	1.15	1.08	1.16	1.16	1.04	1.17	1.09	1.06	0.93	2.00	0.97	0.95	0.86	0.96	1.10
Er	3.26	3.34	3.18	3.24	3.35	3.40	3.12	3.27	3.10	3.34	3.32	2.91	3.35	3.12	3.06	2.82	5.83	2.80	2.89	2.51	2.95	3.18
Tm	0.45	0.46	0.44	0.45	0.47	0.47	0.43	0.45	0.43	0.46	0.46	0.40	0.46	0.43	0.43	0.46	0.98	0.45	0.48	0.42	0.49	0.54
Yb	3.04	3.10	2.98	3.02	3.13	3.17	2.93	3.05	2.89	3.12	3.10	2.65	3.11	2.95	2.87	2.92	5.66	2.79	2.76	2.61	2.74	3.12
Lu	0.43	0.44	0.42	0.43	0.45	0.45	0.42	0.43	0.41	0.44	0.44	0.37	0.44	0.42	0.41	0.41	0.77	0.42	0.41	0.37	0.42	0.45
Hf	6.55	6.44	6.20	7.24	5.98	7.12	6.62	7.09	6.10	7.05	6.70	1.85	7.05	6.56	6.98	4.81	5.03	5.97	4.84	5.09	4.75	4.98
Ta	1.29	1.35	1.03	1.20	1.59	1.21	1.10	1.26	0.97	1.21	1.13	1.16	1.24	1.12	1.13	1.19	1.26	1.09	1.11	1.05	1.01	1.32
Pb	19.61	29.52	25.13	19.32	28.12	19.97	22.22	19.62	20.66	22.40	26.64	21.18	21.94	22.58	17.77	14.30	49.20	17.10	15.80	58.50	55.50	12.30
Th	17.26	18.16	17.52	16.60	15.72	17.66	16.25	16.59	15.81	17.13	15.67	16.01	16.85	16.31	16.08	11.00	10.90	12.00	10.90	9.63	7.96	13.30
U	2.41	2.77	2.60	3.17	2.78	2.47	1.91	2.32	2.11	2.24	1.89	2.16	2.50	2.34	2.09	1.99	2.02	1.56	1.98	1.71	1.21	1.73
Eu/Eu*	0.50	0.52	0.52	0.54	0.54	0.52	0.57	0.53	0.56	0.53	0.51	0.57	0.52	0.53	0.57	0.68	0.26	0.69	0.82	0.76	0.63	0.62
Sr–Nd–Pb isotope compositions																						
$^{87}Rb/^{86}Sr$	1.930861	2.099008	2.001675	1.716520	1.611401	1.683068	1.590512	1.770359	1.543179	1.846611	1.745523	1.604461	1.727026	1.717801	1.712846							
$(^{87}Sr/^{86}Sr)m$	0.709241	0.709396	0.708911	0.709038	0.708775	0.708822	0.708688	0.708923	0.708626	0.708922	0.708911	0.708706	0.708829	0.70883	0.708838							
2SE	9	9	10	9	9	10	6	14	12	11	8	8	9	8	9							
$(^{87}Sr/^{86}Sr)i$	0.706481	0.706395	0.706050	0.706584	0.706471	0.706416	0.706392	0.706414	0.706427	0.706290	0.706423	0.706290	0.706419	0.706368	0.706397							
$^{147}Sm/^{144}Nd$	0.119797	0.115389	0.115626	0.118146	0.119239	0.119340	0.120581	0.117896	0.119926	0.120618	0.120305	0.120092	0.118846	0.116877	0.121338							
$(^{143}Nd/^{144}Nd)m$	0.512365	0.512374	0.512368	0.512377	0.512409	0.512385	0.512385	0.512369	0.512395	0.512374	0.512384	0.512416	0.512392	0.512378	0.512387							
2SE	7	9	10	9	8	8	15	10	10	8	15	14	13	16	12							
$\varepsilon_{Nd}(t)$	−4.34	−4.11	−4.23	−4.08	−3.47	−3.94	−4.27	−3.73	−4.17	−3.98	−3.35	−4.44	−3.80	−4.05	−3.93							
$(^{143}Nd/^{144}Nd)i$	0.51229	0.51230	0.51229	0.51230	0.51233	0.51231	0.51229	0.51231	0.51230	0.51230	0.51234	0.51228	0.51231	0.51230	0.51231							
T_{DM}/Ga	1.27	1.20	1.21	1.23	1.19	1.23	1.28	1.20	1.26	1.25	1.20	1.29	1.22	1.21	1.26							
T_{2DM}/Ga	1.25	1.24	1.24	1.23	1.18	1.22	1.24	1.20	1.24	1.22	1.17	1.26	1.21	1.23	1.21							
$^{206}Pb/^{204}Pb$	18.713	18.658	18.676	18.710	18.656	18.702	18.658	18.703	18.668	18.690	18.684	18.682	18.686	18.674	18.725							
2SE	5	4	5	6	4	7	8	7	5	5	6	5	7	7	8							
$^{207}Pb/^{204}Pb$	15.671	15.669	15.667	15.670	15.674	15.668	15.668	15.671	15.670	15.671	15.666	15.669	15.671	15.668	15.673							
2SE	5	4	5	6	5	6	7	6	5	5	6	5	8	6	8							
$^{208}Pb/^{204}Pb$	39.092	39.026	39.038	39.092	39.030	39.072	39.038	39.084	39.044	39.073	39.049	39.063	39.061	39.038	39.115							
2SE	13	13	15	16	13	17	20	18	15	14	15	14	20	17	22							
$(^{206}Pb/^{204}Pb)_i$	18.699	18.648	18.665	18.691	18.645	18.688	18.648	18.690	18.657	18.679	18.676	18.671	18.673	18.663	18.711							

Table 2 continued

Sample	Granite															Dioritic enclave						
Rock-type	HKV-01	HKV-02	HKV-03	HKV-04	HKV-05	HKV-06	HKV-07	HKV-08	HKV-03	HKV-05	HKV-06	HKV-10	HKV-11	HKV-12	HKV-15	AD-1	AD-2	AD-2	AD-4	AD-5	AD-6	AD-7
$(^{207}Pb/^{204}Pb)_i$	15.661	15.661	15.658	15.656	15.666	15.657	15.661	15.661	15.661	15.662	15.660	15.661	15.661	15.659	15.663							
$(^{208}Pb/^{204}Pb)_i$	38.774	38.803	38.786	38.781	38.827	38.751	38.773	38.777	38.766	38.796	38.836	38.790	38.783	38.777	38.787							

LOI = loss on ignition; $Mg\# = 100 \times Mg^{2+}/(Mg^{2+}+TFe^{2+})$; A/CNK = molecular $Al_2O_3/(CaO + Na_2O + K_2O)$; A/NK = molecular $Al_2O_3/(Na_2O + K_2O)$. $Eu/Eu^* = 2*Eu_N/(Sm_N + Gd_N)$, the subscript of N means normalized to chondrite. m measured isotopic ratios; i are initial values; ($CHUR$ chondritic uniform reservoir), TDM represents the age of crustal material separated from depleted mantle, TDM2 represents the two-stage Nd depleted-mantle model age. $(^{87}Sr/^{86}Sr)_i = (^{87}Sr/^{86}Sr)_m - (^{87}Rb/^{86}Sr) \times (e^{\lambda T}-1)$, $\lambda_{Rb-Sr} = 0.0142\ Ga^{-1}$, $^{87}Rb/^{86}Sr = (Rb/Sr) \times 2.8956$. $(^{143}Nd/^{144}Nd)_i = (^{143}Nd/^{144}Nd)_m - (^{147}Sm/^{144}Nd)_m \times (e^{\lambda T}-1)$, $\lambda_{Sm-Nd} = 0.00654\ Ga^{-1}$, $^{147}Sm/^{144}Nd = (Sm/Nd) \times 0.60456$. $\varepsilon_{Nd}(t) = [(^{143}Nd/^{144}Nd)_{Sample}(t)/(^{143}Nd/^{144}Nd)_{CHUR}(t) - 1] \times 10^4$, $(^{143}Nd/^{144}Nd)_{CHUR}(T) = 0.512638-0.1967 \times (e^{\lambda t}-1)$. $T_{DM} = 1/\lambda_{Sm-Nd} \times \ln \{1 + [((^{143}Nd/^{144}Nd)m - 0.51315)/((^{147}Sm/^{144}Nd)_{Sample} - 0.2137)]\}$
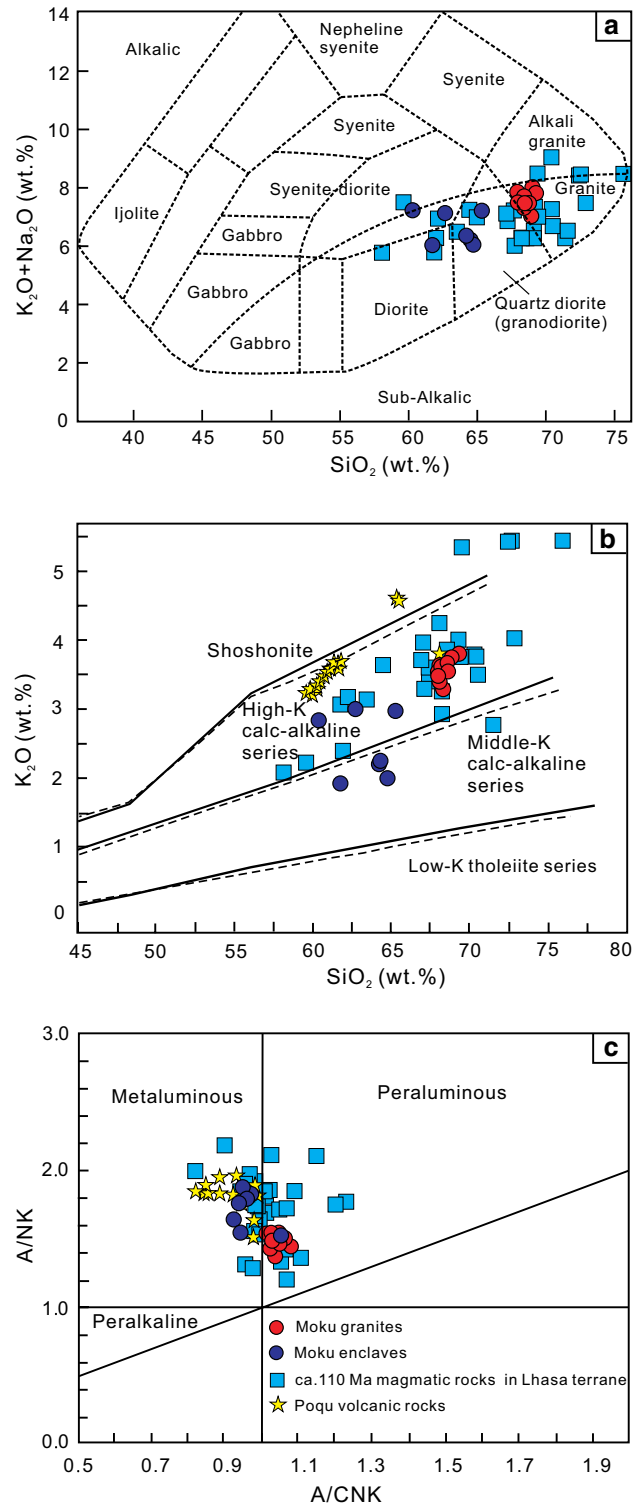
Fig. 4 **a** Total alkalis versus silica diagram (Wilson 1989); **b** SiO₂ versus K₂O diagram (Peccerillo and Taylor 1976); **c** A/NK versus A/CNK diagram (Maniar and Piccoli 1989). Data sources: ca. 110 Ma magmatic rocks in the Lhasa Terrane (Zhu et al. 2009a; Sui et al. 2013; Li et al. 2011; Zhang et al. 2010, 2011, 2012b), Poqu volcanic rocks (Li et al. 2015a)
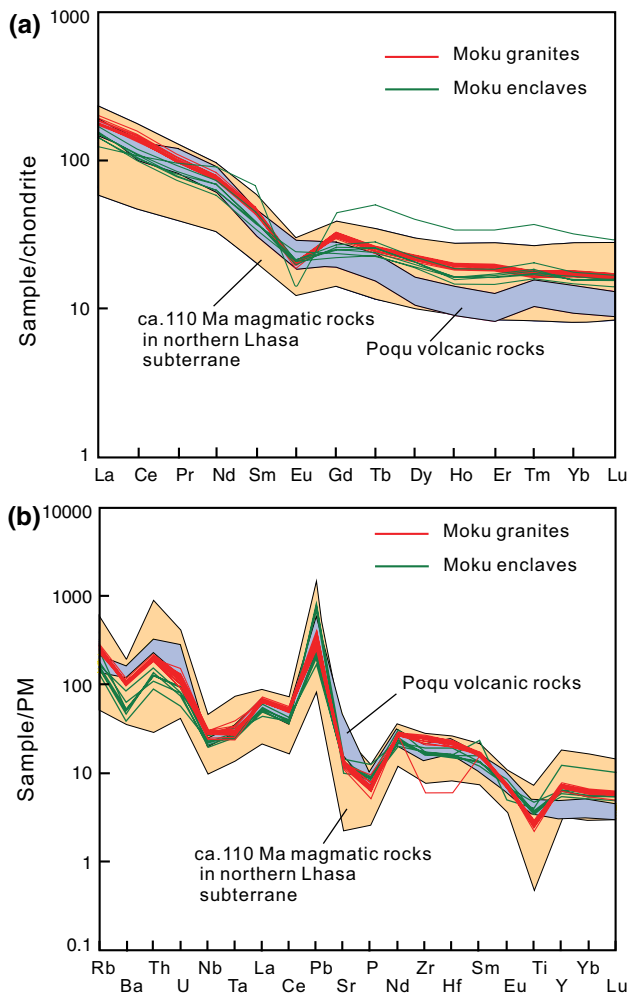
Fig. 5 Chondrite-normalized REE patterns (**a**) and primitive-mantle-normalized trace element patterns (**b**) for the Moku granites and dioritic enclaves. Data sources are same as in Fig. 4
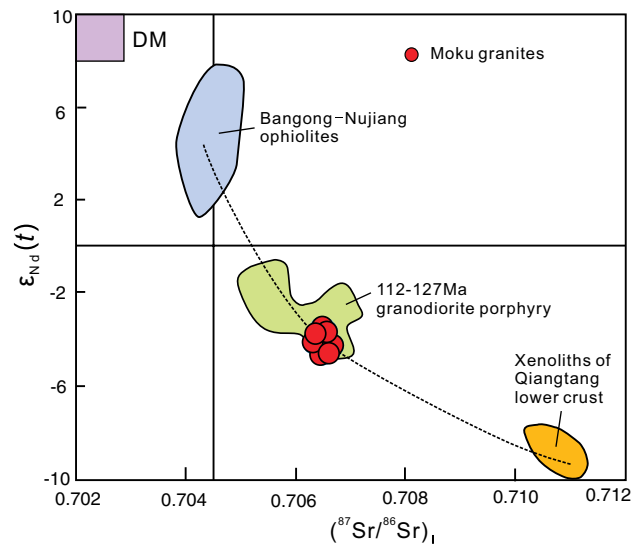

Fig. 6 Plot of $\varepsilon_{Nd}(t)$ versus ($^{87}Sr/^{86}Sr)_i$ diagrams for Moku granites. Data sources: Bangong–Nujiang Ocean basalts (Zhang 2007; Bao et al. 2007), xenoliths of Qiangtang lower crust (Lai and Qin 2008), granodiorite porphyry (112–127 Ma) (Qu and Xin 2006; Xin et al. 2009; Li et al. 2013b, 2016a)
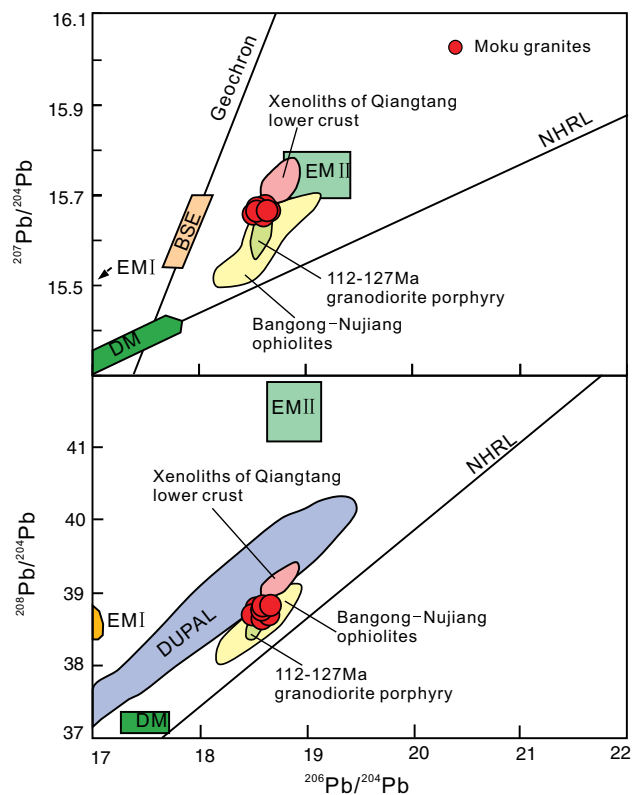

Fig. 7 Plots of $^{207}Pb/^{204}Pb$ and $^{208}Pb/^{204}Pb$ versus $^{206}Pb/^{204}Pb$. Base map is after Zhao et al. (2009). Other data sources are the same as in Fig. 6

Petrogenesis

In general, three mechanisms have been proposed for the petrogenesis of intermediate to felsic I-type granites: (1) remelting of preexisting infra-crustal igneous rocks or metamorphic rocks (Chappell and Stephens 1988; Chappell and White 2001; Griffin et al. 2002; Wu et al. 2007); (2) advanced fractional crystallization of mantle-derived parental magma (Cawthorn and Brown 1976; Wyborn et al. 2001; Chiaradia 2009; Li et al. 2009b); and (3) the mixing of the melts from partial melting of crustal rocks and mantle-derived magmas (Kemp et al. 2007; Collins and Richards 2008; Li et al. 2009a; Zhu et al. 2009a, c; Wang et al. 2014).

Dioritic enclaves within coeval host rocks can provide significant evidence for petrogenesis of I-type granites

Table 3 Zircons Hf isotopic data of the Moku granites and dioritic enclaves

Spot	Ages (Ma)	^{176}Yb/^{177}Hf	^{176}Lu/^{177}Hf	^{176}Hf/^{177}Hf	2σ	$\varepsilon_{Hf}(0)$	εHf(t)	T$_{DM}$ (Ga)	T$_{DM}^{C}$ (Ga)	f$_{Lu/Hf}$
UKG, host granite, 100.3 ± 0.6 Ma, εHf(t) = −13.8 to +2.6 (19 analyses)										
1. UKG-01	101	0.062307	0.001902	0.282752	0.000021	−0.7	1.4	0.73	1.00	−0.94
2. UKG-05	101	0.057546	0.001831	0.282787	0.000032	0.5	2.6	0.68	0.93	−0.94
3. UKG-06	102	0.040620	0.001342	0.282685	0.000027	−3.1	−0.9	0.81	1.14	−0.96
4. UKG-07	100	0.039100	0.001271	0.282323	0.000030	−15.9	−13.8	1.32	1.88	−0.96
5. UKG-09	98	0.036763	0.001253	0.282735	0.000024	−1.3	0.8	0.74	1.03	−0.96
6. UKG-10	99	0.038797	0.001238	0.282655	0.000023	−4.1	−2.0	0.85	1.20	−0.96
7. UKG-11	100	0.063828	0.002122	0.282691	0.000031	−2.9	−0.8	0.82	1.13	−0.94
8. UKG-14	99	0.025000	0.000859	0.282768	0.000027	−0.1	2.0	0.68	0.96	−0.97
9. UKG-15	101	0.041907	0.001487	0.282752	0.000034	−0.7	1.4	0.72	1.00	−0.96
10. UKG-17	100	0.040677	0.001322	0.282731	0.000028	−1.5	0.6	0.75	1.04	−0.96
11. UKG-18	102	0.045907	0.001566	0.282763	0.000027	−0.3	1.8	0.70	0.97	−0.95
12. UKG-19	101	0.051898	0.001826	0.282776	0.000048	0.2	2.3	0.69	0.95	−0.94
13. UKG-20	102	0.045667	0.001501	0.282742	0.000023	−1.1	1.1	0.73	1.02	−0.95
14. UKG-21	100	0.076914	0.002443	0.282678	0.000032	−3.3	−1.3	0.85	1.15	−0.93
15. UKG-22	99	0.045287	0.001477	0.282684	0.000021	−3.1	−1.0	0.82	1.14	−0.96
16. UKG-23	100	0.072772	0.002463	0.282688	0.000031	−3.0	−0.9	0.83	1.13	−0.93
17. UKG-24	101	0.040594	0.001394	0.282744	0.000031	−1.0	1.1	0.73	1.01	−0.96
18. UKG-25	98	0.048354	0.001674	0.282576	0.000034	−6.9	−4.9	0.97	1.36	−0.95
19. UKG-26	101	0.049705	0.001669	0.282728	0.000023	−1.5	0.6	0.76	1.05	−0.95
HKV, host granite, 100.6 ± 0.5 Ma, εHf(t) = −24.4 to +2.2 (20 analyses)										
1. HKV-02	101	0.039635	0.001271	0.282719	0.000021	−1.9	0.2	0.76	1.07	−0.96
2. HKV-03	100	0.051375	0.001569	0.282755	0.000019	−0.6	1.5	0.72	0.99	−0.95
3. HKV-04	101	0.031100	0.001001	0.282021	0.000017	−26.6	−24.4	1.73	2.50	−0.97
4. HKV-05	101	0.035104	0.001224	0.282774	0.000022	0.1	2.2	0.68	0.95	−0.96
5. HKV-06	100	0.048930	0.001537	0.282705	0.000018	−2.4	−0.3	0.79	1.09	−0.95
6. HKV-07	101	0.044720	0.001426	0.282727	0.000018	−1.6	0.5	0.75	1.05	−0.96
7. HKV-08	101	0.040257	0.001230	0.282727	0.000016	−1.6	0.5	0.75	1.05	−0.96
8. HKV-10	101	0.041779	0.001379	0.282713	0.000018	−2.1	0.0	0.77	1.08	−0.96
9. HKV-11	101	0.043130	0.001417	0.282769	0.000018	−0.1	2.0	0.69	0.96	−0.96
10. HKV-13	101	0.050226	0.001602	0.282755	0.000018	−0.6	1.5	0.72	0.99	−0.95
11. HKV-15	100	0.048326	0.001489	0.282738	0.000017	−1.2	0.9	0.74	1.03	−0.96
12. HKV-17	100	0.052465	0.001678	0.282716	0.000021	−2.0	0.1	0.77	1.07	−0.95
13. HKV-19	101	0.047686	0.001545	0.282711	0.000017	−2.2	−0.1	0.78	1.08	−0.95
14. HKV-20	100	0.058543	0.001897	0.282752	0.000019	−0.7	1.4	0.73	1.00	−0.94
15. HKV-21	102	0.050121	0.001658	0.282716	0.000016	−2.0	0.2	0.77	1.07	−0.95
16. HKV-22	102	0.036001	0.001205	0.282691	0.000014	−2.9	−0.7	0.80	1.12	−0.96
17. HKV-23	100	0.034571	0.001149	0.282698	0.000016	−2.6	−0.5	0.79	1.11	−0.97
18. HKV-24	102	0.042091	0.001386	0.282585	0.000017	−6.6	−4.5	0.95	1.34	−0.96
19. HKV-25	102	0.045894	0.001502	0.282723	0.000016	−1.7	0.4	0.76	1.06	−0.95
20. HKV-26	100	0.040429	0.001366	0.282749	0.000016	−0.8	1.3	0.72	1.00	−0.96
Sample BT-9 dioritic enclave, 100.3 ± 0.8 Ma, εHf(t) = −13.3 to +3.6 (10 analyses)										
1. BT-9-19	100	0.045328	0.001606	0.282771	0.000036	−0.1	2.0	0.69	0.96	−0.95
2. BT-9-21	101	0.063398	0.002186	0.282339	0.000124	−15.3	−13.3	1.33	1.85	−0.93
3. BT-9-23	100	0.042256	0.001493	0.282805	0.000077	1.2	3.3	0.64	0.89	−0.96
4. BT-9-29	101	0.046085	0.001611	0.282643	0.000050	−4.6	−2.5	0.88	1.22	−0.95
5. BT-9-30	101	0.016887	0.000543	0.282614	0.000115	−5.6	−3.4	0.89	1.28	−0.98
6. BT-9-35	100	0.051113	0.001791	0.282689	0.000035	−2.9	−0.8	0.81	1.13	−0.95

Table 3 continued

Spot	Ages (Ma)	$^{176}Yb/^{177}Hf$	$^{176}Lu/^{177}Hf$	$^{176}Hf/^{177}Hf$	2σ	$\varepsilon_{Hf}(0)$	$\varepsilon Hf(t)$	T_{DM} (Ga)	T_{DM}^C (Ga)	$f_{Lu/Hf}$
7. BT-9-36	101	0.056762	0.001977	0.282671	0.000056	−3.6	−1.5	0.85	1.17	−0.94
8. BT-9-38	100	0.036036	0.001223	0.282662	0.000034	−3.9	−1.8	0.84	1.18	−0.96
9. BT-9-39	100	0.039744	0.001408	0.282674	0.000028	−3.5	−1.4	0.83	1.16	−0.96
10. BT-9-42	100	0.048988	0.001787	0.282814	0.000054	1.5	3.6	0.63	0.87	−0.95

$\varepsilon_{Hf}(t) = 10{,}000 \times \{[(^{176}Hf/^{177}Hf)_S - (^{176}Lu/^{177}Hf)m \times (e^{\lambda t} - 1)]/[(^{176}Hf/^{177}Hf)_{CHUR,0} - (^{176}Lu/^{177}Hf)_{CHUR} \times (e^{\lambda t} - 1)] - 1\}$. $TDM = 1/\lambda \times \ln\{1 + [(^{176}Hf/^{177}Hf)m - (^{176}Hf/^{177}Hf)_{DM}]/[(^{176}Lu/^{177}Hf)_m - (^{176}Lu/^{177}Hf)_{DM}]\}$. $T_{DMC} = T_{DM} - (T_{DM} - t) \times [(f_{cc} - f_m)/(f_{cc} - f_{DM})]$. $f_{Lu/Hf} = (^{176}Lu/^{177}Hf)_m/(^{176}Lu/^{177}Hf)_{CHUR} - 1$. $\lambda = 1.867 \times 10^{-11}/a$; $(^{176}Lu/^{177}Hf)_{CHUR} = 0.0332$, $(^{176}Hf/^{177}Hf)_{CHUR,0} = 0.282772$; $(^{176}Lu/^{177}Hf)_{DM} = 0.0384$, $(^{176}Hf/^{177}Hf)_{DM} = 0.28325$; $(^{176}Lu/^{177}Hf)_{mean\ crust} = 0.015$; $f_{cc} = [(^{176}Lu/^{177}Hf)_{mean\ crust}/(^{176}Lu/^{177}Hf)_{CHUR}] - 1$; $f_s = f_{Lu/Hf}$; $f_{DM} = [(^{176}Lu/^{177}Hf)_{DM}/(^{176}Lu/^{177}Hf)_{CHUR}] - 1$; m measured isotopic ratios

(Didier 1984; Vernon 1984; Li 2002; Mo et al. 2007; Yang et al. 2007; Li et al. 2009a; Zhang et al. 2012b). Although abundant dioritic enclaves are observed in the Moku granite, many models have been proposed to explain the origin of the enclaves, including residual materials of the initial magma, xenoliths of surrounding rocks, magmatic precipitation, or remnants of a mafic component added to granitic magma (magma mixing) (Chappell and Simpson 1984; Chappell and White 1992; Didier 1987; Holden et al. 1987; Yang et al. 2004; Guan et al. 2012). The dioritic enclaves within the Moku granites are generally spheroidal to ellipsoidal or ovoidal with typical magmatic textures and coeval with the host granites; thus, they cannot be the products of residual materials of the initial magma or xenoliths of surrounding rocks. Meanwhile, the dioritic enclaves contain K-feldspar megacrysts; this unbalanced mineral combination suggests the mixing of mafic and felsic magmas before cooling and crystallization (Silva et al. 2000; Mo et al. 2007; Karsli et al. 2007, 2010; Kaygusuz and Aydincakir 2009). Moreover, plagioclases of the enclaves display typical oscillatory zoning textures, and no cumulate textures are found in the dioritic enclaves. These features too can be attributed to magma mixing (Hibbard 1991; Waight et al. 2000) and clearly rule out any strictly cogenetic origin. In addition, a light-colored felsic halo occurs at the edges of the enclaves, which reflects the product of the mixing of basic and granitic magmas (Fig. 2c) (Mo et al. 2007). In summary, petrographic characteristics of the dioritic enclaves provide robust evidence that the Moku granites were generated by mixing between mantle-derived mafic magmas and felsic magmas.

The TiO$_2$, MgO, Fe$_2$O$_3^T$, P$_2$O$_5$, and CaO contents of the Moku granites and hosted enclaves show a negative correlation with SiO$_2$ (Fig. 8). These are typical characteristics of magma mixing rather than fractional crystallization (Zorpi et al. 1991; Karsli et al. 2007; Kaygusuz and Aydincakir 2009; Zhang et al. 2009). In the FeO^T versus MgO diagram (Fig. 8f), the Moku granites and dioritic enclaves extend along a magma mixing trend (Zorpi et al. 1991), indicating that the Moku magma was derived from mixing

between mantle magma and crustal melts. Moreover, the Moku granites and dioritic enclaves have high Mg$^\#$ values (37.46–40.84 and 43.20–50.90, respectively), higher than those of pure crustal melts (Sisson et al. 2005), which suggest that mantle-derived magma was mixed into the crustal melts during generation of the Moku magma. The host granites have major elements that are clearly different from those of the enclaves, but the two rock types display similar rare earth element and trace element patterns. This type of composition is considered as an indicator of magma mixing (Yang et al. 2007; Zhang et al. 2011). Moreover, the enclaves are composed of a variety of rock types including syenite-diorite, diorite and quartz diorite, but they have similar trace element contents and patterns (Figs. 4a, 5). These features are considered as the results of homogenization between basic and acidic melts during magma mixing; a similar phenomenon is also observed in the ca. 110 Ma granites from the northern Lhasa subterrane (Zhang et al. 2010, 2011, 2012b).

The Lu–Hf isotope system of zircons has high closure temperatures (Cherniak et al. 1997; Cherniak and Watson 2003), so that partial melting or fractional crystallization cannot affect the Hf isotopic ratios. Therefore, zircon Hf isotopic compositions can differentiate between magma mixing and fractional crystallization processes (Griffin et al. 2002; Kemp and Hawkesworth 2006; Wu et al. 2007). In general, negative $\varepsilon_{Hf}(t)$ values and old Hf model ages (T_{DM}^C) indicate that the magmas were derived by anatexis or remelting of the ancient continental crust (Allègre and Ben 1980; Wang et al. 2014). In contrast, relatively high $\varepsilon_{Hf}(t)$ values and younger T_{DM}^C suggest the magmas are most likely derived from a mantle source or recycled juvenile crust (Jahn et al. 2000; Mo et al. 2007; Hou et al. 2013). Most of the zircons from the Moku granites have negative $\varepsilon_{Hf}(t)$ values and ancient T_{DM}^C (Table 3), suggesting that they were derived from anatexis or remelting of ancient continental crust. However, the wide variation of $\varepsilon_{Hf}(t)$ (−24.4 to 2.6) and T_{DM}^C (0.93–2.50 Ga) (Fig. 9) indicates open-system processes involving more radiogenic (i.e., mantle-derived) and less radiogenic (i.e., crustal)
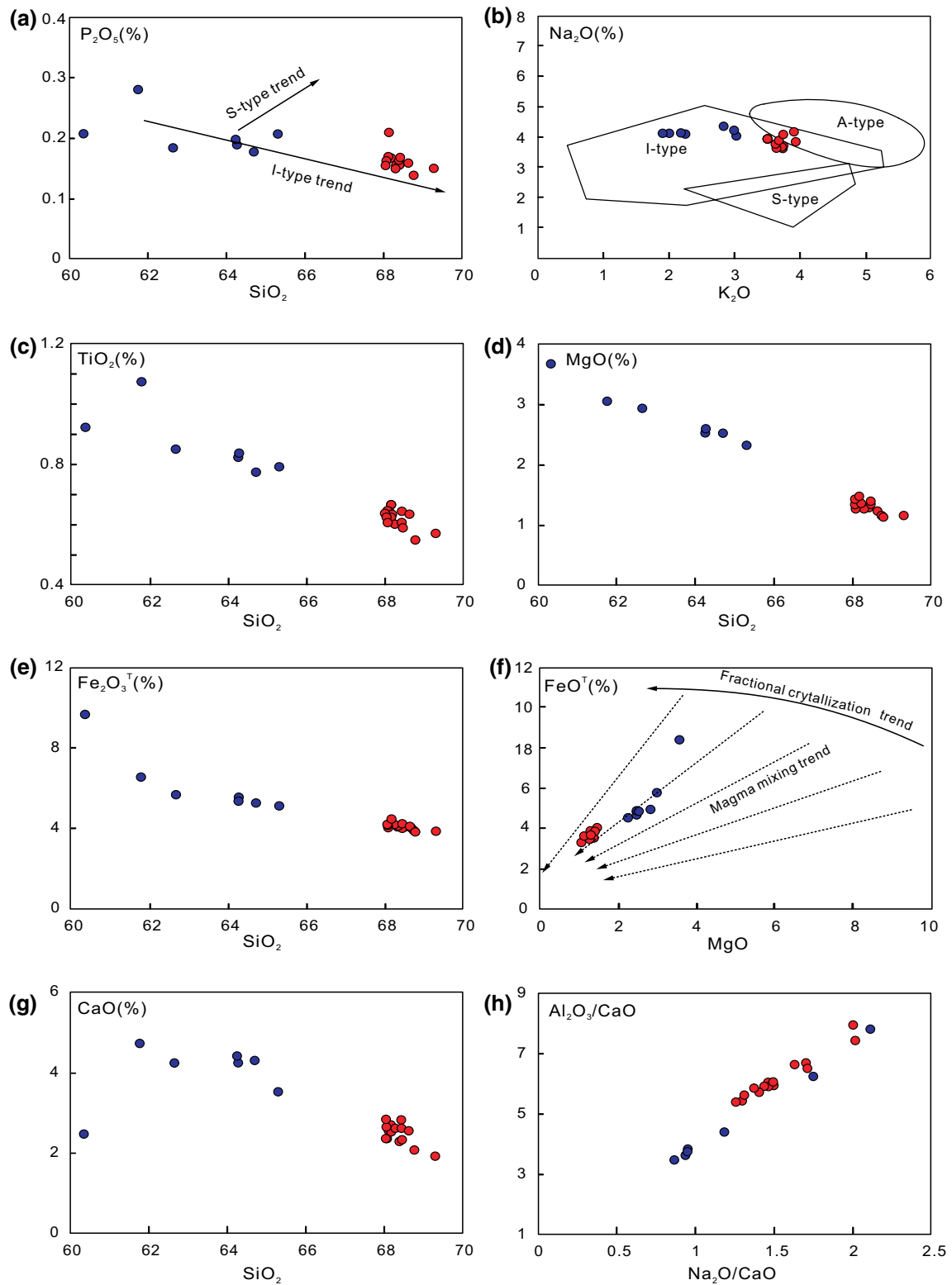
Fig. 8 Selected geochemical plots of the Moku granites and dioritic enclaves
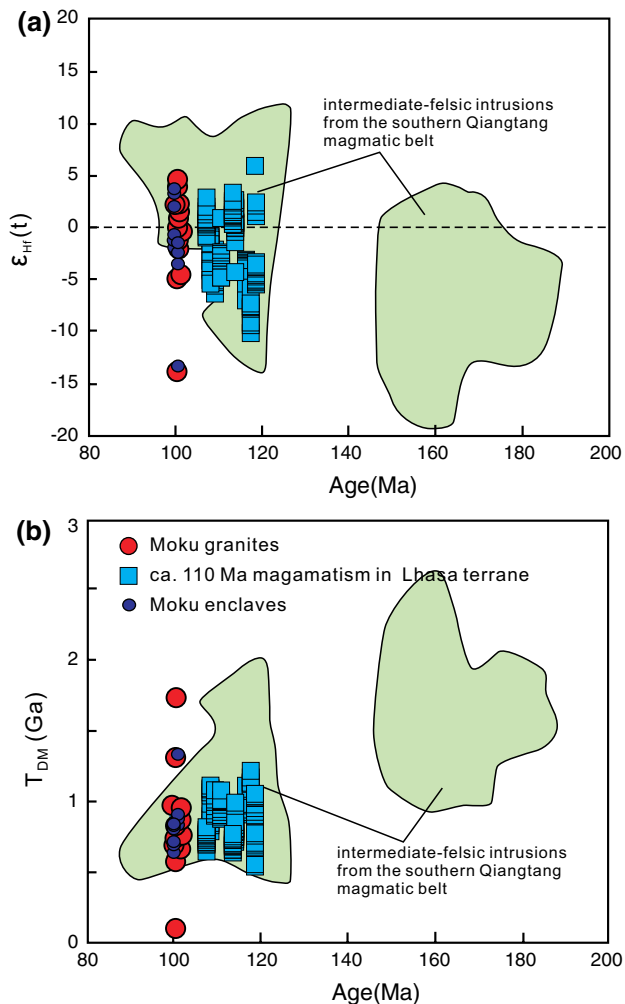
Fig. 9 Plots of $\varepsilon_{Hf}(t)$–ages (**a**) and T_{DM}–ages (**b**) against ages of the Moku granites and dioritic enclaves. Date for the intermediate-felsic intrusions of the southern Qiangtang magmatic belt is from Li et al. (2013a, 2016a) and Liu et al. (2015). Date for the ca. 110 Ma rocks in northern Lhasa subterrane is from Zhu et al. (2009a, 2011) and Zhang et al. (2010)

end-members (Bolhar et al. 2008). This hypothesis is supported by the presence of dioritic enclaves within the Moku granites. In addition, the dioritic enclaves have variable $\varepsilon_{Hf}(t)$ values (−13.3 to +3.6) and T_{DM}^{C} (0.87–1.85 Ga) (Fig. 9). These features are different from those of a magma derived from a single source with a homogeneous Hf isotopic composition (Griffin et al. 2002; Kemp et al. 2007), which indicates the involvement of mantle-derived materials in the source of the Moku magma. The variable $\varepsilon_{Hf}(t)$ and T_{DM}^{C} are similar to those of the intermediate-felsic intrusions from the southern Qiangtang magmatic belt and ca. 110 Ma igneous rocks in the northern Lhasa subterrane (Fig. 9), which are considered to be the results of magma mixing between lower crustal melts and rising asthenospheric melts (Zhu et al. 2006a, 2009a, 2011,

2013, 2016; Ma and Yue 2010; Sui et al. 2013; Li et al. 2013b, 2016a; Liu et al. 2015).

The Moku granites have high $(^{87}Sr/^{86}Sr)_i$ values (0.70605–0.70658), negative $\varepsilon_{Nd}(t)$ (−3.35 to −4.44), old Nd model ages (1.19–1.29 Ga), and Pb isotopic characteristics identical to those of the Bangong–Nujiang ophiolites (Fig. 7), which suggests that the Moku magma may derive from a dominantly lower crustal source with contributions from an asthenospheric mantle component. Regarding the source of the Moku granites, the lower crustal mafic granulitic xenoliths of the Qiangtang Terrane (Lai and Qin 2008) presumably represent the lower crust beneath this region, and the Bangong–Nujiang ophiolites (Zhang 2007; Bao et al. 2007) represent the asthenospheric mantle composition with respect to the Sr–Nd isotopic composition. In the $\varepsilon_{Nd}(t)$ versus $(^{87}Sr/^{86}Sr)_i$ diagram (Fig. 6), the Moku granites plot in the field adjacent to the mixing line between asthenospheric mantle composition and the lower crustal components, which suggest that these rocks were derived from mixing between asthenospheric mantle and lower crustal materials. These results are similar to those of the 112–127 Ma granodiorite porphyries in the Qiangtang Terrane (Fig. 6), which were derived from magma mixing between melts derived from the lower crust and basaltic melts derived from the metasomatized mantle wedge (Qu and Xin 2006; Xin et al. 2009; Li et al. 2013b, 2016a). Thus, it can be inferred that the Moku magma originated by the anatexis of the Qiangtang lower crust and basaltic melts derived from rising asthenosphere mantle.

Basaltic melts derived from rising asthenosphere could well explain the aluminum saturation index of the Moku granites (A/CNK 1.01–1.08). In general, lower crustal melts are peraluminous (A/CNK > 1.1), and mantle-derived melts are calc-alkaline (A/CNK < 1) (Zhang et al. 2010). The Moku granites are quasi-aluminous rocks (1 < A/CNK < 1.1) because of the mixing between lower crustal melts and basaltic melts derived from rising asthenospheric mantle. In this model, the rising asthenosphere can also provide the necessary heat for dehydration melts derived from the lower crust and produce granitic magma. Moreover, the occurrence of magma mixing is confirmed by the Pb isotopic compositions. In the $^{207}Pb/^{204}Pb$ versus $^{206}Pb/^{204}Pb$ and $^{208}Pb/^{204}Pb$ versus $^{206}Pb/^{204}Pb$ diagrams, the Moku granites plot in the field between the Bangong–Nujiang ophiolites and the Qiangtang lower crust (Fig. 7). Therefore, we conclude that the Moku magma was generated by mixing between lower crustal melts and mantle-derived basaltic magmas.

In summary, the geochemical data of the major and trace elements, together with the Sr–Nd–Pb–Hf isotopic compositions, suggest that the source of the Moku granites was derived from a mixture of asthenospheric mantle-derived magma and anatexis of the Qiangtang lower crust. This

implies that the petrogenesis of the Moku granites is in accordance with the ca. 110 Ma igneous rocks in the northern Lhasa subterrane (Zhu et al. 2006a, 2009a, 2011, 2013, 2016; Ma and Yue 2010; Sui et al. 2013).

Geodynamic mechanism

It is generally accepted that the final closing of the Bangong–Nujiang Ocean and the subsequent Lhasa–Qiangtang collision occurred during the Early Cretaceous (Girardeau et al. 1984; Xu et al. 1985; Dewey et al. 1988; Kapp et al. 2005; Zhu et al. 2006a, 2009a, 2016; Leier et al. 2007; Zhang et al. 2012a; Li et al. 2015b). In the Moku area, the angular unconformity between the continental Abushan Formation and the underlying marine deposits marks the Lhasa–Qiangtang collision (Li et al. 2015a). The Moku pluton intruded into the Abushan Formation and is coeval with the volcanic layers (96–102 Ma) in the lower part of this formation (Li et al. 2015a), which implies that the pluton emplacement was contemporary with or occurred shortly after the Lhasa–Qiangtang collision.

All of the Moku samples display high-K calc-alkaline series, LREE-rich patterns, enrichment of LILE, and depletion of HFSE. Their geochemical characteristics are consistent with arc-type magmas (Pearce et al. 1984; Wilson 1989; Condie 2005). However, the ages and geological background indicate that the emplacement of the Moku pluton lagged behind the subduction of the Bangong–Nujiang Ocean. Therefore, an island or continental arc model for subduction-related magmatism is excluded in space and time. Moreover, the coeval dioritic enclaves exhibit weak depletion of Nb, negative Sr anomalies (Fig. 5b), and high Zr abundances (182–218×10^{-6}) (Table 2), which are different from arc-related rocks that display strong depletion of Nb, normal Sr concentrations, and low Zr contents ($Zr < 50 \times 10^{-6}$).

Based on the geochemical characteristics of major and trace elements but lacking any isotopic data, Li et al. (2015a) suggested that the Poqu and Madeng volcanic rocks were derived by the partial melting of relict subducted oceanic crust combined with the input of oceanic sediments. The Moku granites show similar geochemical characteristics (i.e., high-K calc-alkaline series, enrichments in LILE and LREE, and depletions in HFSE) to the coeval Poqu and Madeng volcanic rocks (Fig. 5), implying that they have an analogous origin. Nevertheless, if the granites originated as subducted slab melts, they should have mid-ocean-ridge basalt (MORB)-like Sr–Nd isotopic compositions ($\varepsilon_{Nd} \approx 10$) (Defant and Drummond 1990). In contrast, the Moku granites exhibit much more evolved isotopic compositions ($\varepsilon_{Nd} = -4.35$ to -4.4; $^{87}Sr/^{86}Sr = 0.70605$–$0.70658$), which are distinctly different from oceanic (MORB and OIB) basalts. Moreover, arc
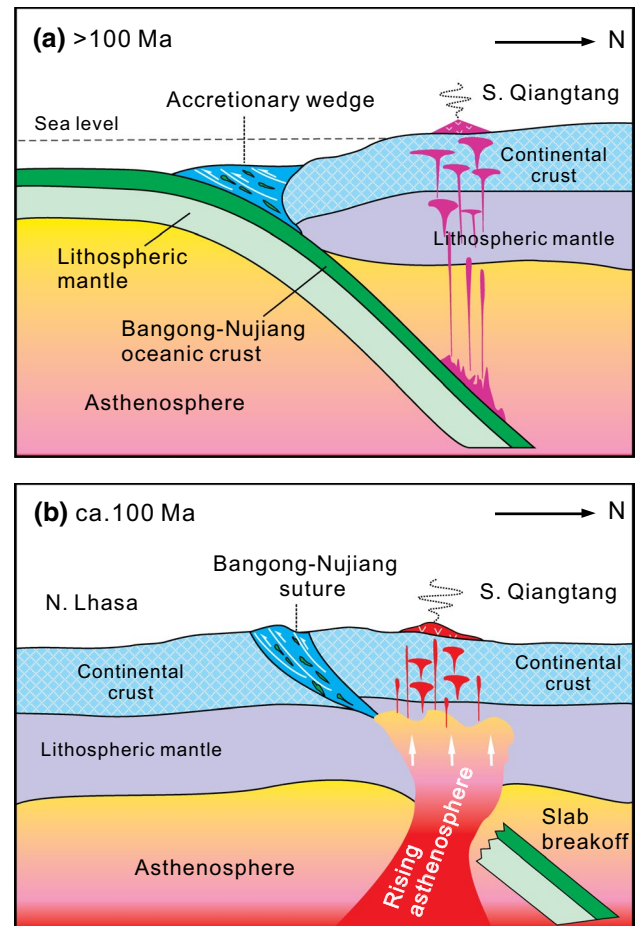

Fig. 10 Simplified geodynamic model showing the magmatisms of the Qiangtang Terrane during Early Cretaceous. a The Bangong–Nujiang oceanic lithosphere subducted beneath the Qiangtang Terrane and resulted in arc-related magmatic rocks. b The northward subduction of the Bangong–Nujiang oceanic lithosphere broken off at ca. 100 Ma

volcanic rocks generally have restricted Sr isotope ratios ($^{87}Sr/^{86}Sr = 0.703$–0.704) (Hawkesworth et al. 1993), which contrast significantly with those of the Moku granites.

These granites are also unlikely to have been caused by remelting of a thickened lower crust or lithospheric delamination during the Lhasa–Qiangtang collision. The Lhasa–Qiangtang collision and related remelting of a thickened lower crust had been adopted to interpret the petrogenesis of the Early Cretaceous magmatism in central Tibet (Xu et al. 1985; Pearce and Mei 1988). However, there is no clear evidence that crustal thickening had occurred in central Tibet at ~100 Ma. Moreover, the magma derived from remelting of a thickened lower crust usually lacks mantle components (Zhu et al. 2009a, b), whereas the Moku granites have contributions from mantle-derived components. Previous studies have verified that the partial melting of metabasic igneous

rocks in the eclogite to amphibolite facies in the thickened lower crust (Atherton and Petford 1993; Chung et al. 2003; Wen et al. 2008; Karsli et al. 2010) can produce melts with high Sr and low Y and Yb (adakitic rocks) during collision. However, the ca. 100 Ma magmatic rocks show different characteristics from those of adakitic rocks. In addition, the ca. 100 Ma magmatic rocks were emplaced before delamination magmatism related to the Lhasa–Qiangtang collision (75–79 Ma) (Li et al. 2013a); thus, they cannot be explained by lithospheric delamination.

Excluding the above models, the ca. 100 Ma magmatic rocks were most likely triggered by slab break-off associated with the subduction of the Bangong–Nujiang oceanic lithosphere. It has been accepted that with the final closing of an ocean, the subducted/subducting oceanic slab breaks off during or after collision (von Blanckenburg and Davis 1995; Wong et al. 1997; Zhu et al. 2009a). The slab break-off induces upwelling of the deep asthenosphere, causing mantle decompression melting, and the mantle-derived melt cause crustal anatexis (Zhu et al. 2009a). This geodynamic interpretation for the Moku granites and ~100 Ma volcanic rocks is also supported by the following facts: (1) recent studies show that the Bangong–Nujiang oceanic lithosphere underwent northward subduction (Li et al. 2014b, 2015a, 2016b; Zhu et al. 2016); (2) the ~100 Ma volcanic rocks are almost coeval with the Qiangtang–Lhasa collision; (3) the magmatic rocks were derived from anatexis of the ancient crust that mixed with asthenospheric materials, which is similar to what is predicted by the slab break-off model (Davies and Von Blanckenburg 1995; Dilek and Altunkaynak 2009; Zhu et al. 2009a); and (4) in addition to the ca. 100 Ma magmatic rocks in the Moku area, Early Cretaceous magmatic rocks in the southern Qiangtang subterrane are more widespread than previously thought, including the Rena-Co (109–110 Ma) (Chang et al. 2011) and the Duolong (105 Ma) (Li et al. 2016b).

Based on the above facts and combined with regional evolution, a tectonic scenario for the formation of the Moku granites and coeval volcanic rock in the Moku area can be summarized as follows. Before the Lhasa–Qiangtang collision (> 100 Ma), the Bangong–Nujiang oceanic lithosphere was subducting northward beneath the Qiangtang Terrane, and this resulted in the development of a magmatic arc in the southern Qiangtang subterrane (Fig. 10a) (Li et al. 2014a, 2015a, 2016a; Geng et al. 2016; Zhu et al. 2016). With the Lhasa–Qiangtang collision, the Bangong–Nujiang oceanic lithosphere continued to descend beneath the southern Qiangtang subterrane. At approximately 100 Ma, the Bangong–Nujiang oceanic lithosphere broke off from the subducting slab, causing the upwelling of the asthenospheric magma, which in turn induced anatexis of Qiangtang lower crust and led to the formation of the Moku granites and coeval volcanic rocks (Fig. 10b). Because slab break-off is dominated by the age of oceanic crust, the initial plate convergence rate, and the angle of the subducted oceanic slab (Duretz et al. 2011), this event may have led to the occurrence of magmatism in the southern Qiangtang subterrane (ca. 100 Ma) ~10 Ma later than in the northern Lhasa subterrane (ca. 110 Ma).

Conclusions

1. The Moku pluton was emplaced at ca. 100 Ma and coeval with the hosted dioritic enclaves, marking Early Cretaceous magmatic intrusion in the southern Qiangtang subterrane.
2. The Moku granites are peraluminous and high-K calc-alkaline I-type granites, enriched in LILE and LREE and depleted in HFSE and HREE. Sr–Nd–Pb and zircon Hf isotopic compositions suggest that the granites were derived from the anatexis of the Qiangtang lower crust that mixed with upwelling asthenospheric magma.
3. The Moku pluton and coeval volcanic rocks in the southern Qiangtang subterrane were triggered by the slab break-off of the northward-subducting Bangong–Nujiang oceanic lithosphere during the Lhasa–Qiangtang collision.

References

Allègre CJ, Ben OD (1980) Nd–Sr isotopic relationship in granitoid rocks and continental crust development: a chemical approach to orogenesis. Nature 286:335–342

Allègre CJ, Courtillot V, Tapponnier P et al (1984) Structure and evolution of the Himalaya–Tibet orogenic belt. Nature 307:17–22

Andersen T (2002) Correction of common lead in U-Pb analyses that do not report 204Pb. Chem Geol 192:59–79

Atherton MP, Petford N (1993) Generation of sodium-rich magmas from newly under plated basaltic crust. Nature 362:144–146

Bao PS, Xiao XC, Su L, Wang J (2007) Petrological, geochemical and chronological con-straints for the tectonic setting of the Dongco ophiolite in Tibet. Sci China Ser D 50(5):660–671

Belousova EA, Griffin WL, Shee SR, Jackson SE, O'Reilly SY (2001) Two age populations of zircons from the Timber Creek kimberlites, Northern Territory, as determined by laser-ablation ICP-MS analysis. Aust J Earth Sci 48:757–765

Blichert-Toft J, Albarède F (1997) The Lu–Hf isotope geochemistry of chondrites and the evolution of the mantle-crust system. Earth Planet Sc Lett 148:243–258

Bolhar R, Weaver SD, Whitehouse MJ, Palin JM, Woodhead JD, Cole JW (2008) Sources and evolution of arc magmas inferred from coupled O and Hf isotope systematics of plutonic zircons from the Cretaceous Separation Point Suite (New Zealand). Earth Planet Sci Lett 268:312–324

Cawthorn RG, Brown PA (1976) A model for the formation and crystallization of corundum-normative calc-alkaline magmas through amphibole fractionation. J Geol 84:467–476

Chang QS, Zhu DC, Zhao ZD, Mo XX, Liu YS, Hu ZC (2011) Zircon U–Pb geochronology and Hf isotopes of the early cretaceous Rena-Co rhyolites from southern margin of Qiangtang, Tibet, and their implications. Acta Petrol Sin 27(7):2034–2044 **(in Chinese with English abstract)**

Chappell BW (1999) Aluminium saturation in I-and S-type granites and the characterization of fractionated haplogranites. Lithos 46:535–551

Chappell BW, Simpson PR (1984) Source rocks of I- and S-Type granites in the Lachlan Fold Belt, Southeastern Australia [and Discussion]. Philos Trans R Soc A 310:693–707

Chappell BW, Stephens WE (1988) Origin of infracrustal (I-type) granite magmas. Trans R Soc Edinb Earth 79(2–3):71–86

Chappell BW, White AJR (1992) I- and S-type granites in the Lachlan Fold Belt. Trans R Soc Edinb Earth 83:1–26

Chappell BW, White AJR (2001) Two contrasting granite types: 25 years later. Aust J Earth Sci 48:489–499

Cherniak DJ, Watson EB (2003) Diffusion in zircon. In: Hanchar JM, Hoskin PWO (eds) Zircon. Zircon Reviews of Mineralogy and Geochemistry 53, pp 113–143

Cherniak DJ, Hanchar JM, Watson EB (1997) Diffusion of tetravalent cations in zircon. Contrib Miner Pet 127:383–390

Chiaradia M (2009) Adakite-like magmas from fractional crystallization and melting assimilation of mafic lower crust (Eocene Macuchi arc, Western Cordillera, Ecuador). Chem Geol 265:468–487

Chung SL, Liu DY, Ji JQ, Chu MF, Lee HY, Wen DJ, Lo CH, Lee TY, Qian Q, Zhang Q (2003) Adakites from continental collision zones: melting of thickened lower crust beneath southern Tibet. Geology 31:1021–1024

Collins WJ, Richards SW (2008) Geodynamic significance of S-type granites in circum-Pacific orogens. Geology 36:559–562

Condie KC (2005) High field strength element ratios in Archean basalts: a window to evolving sources of mantle plumes? Lithos 79:491–504

Davies JH, von Blanckenburg F (1995) Slab breakoff: a model of lithospheric detachment and its test in the magmatism and deformation of collisional orogens. Earth Planet Sci Lett 129:85–102

Defant MJ, Drummond MS (1990) Derivation of some modern arc magmas by melting of young subducted lithosphere. Nature 347:662–665

Deng J, Wang QF, Li GJ, Li CS, Wang CM (2014) Tethys tectonic evolution and its bearing on the distribution of important mineral deposits in the Sanjiang region, SW China. Gondwana Res 26(2):419–437

Dewey JF, Shackleton RM, Chang C, Sun Y (1988) The tectonic evolution of the Tibetan plateau. Philos Trans R Soc A 327:379–413

Didier J (1984) The problem of enclaves in granitic rocks: a review of recent ideas on their origin. Science Press, Beijing, pp 137–144

Didier J (1987) Contribution of enclave studies to the understanding of origin and evolution of granitic magmas. Geol Rundsch 76:41–50

Dilek Y, Altunkaynak S (2009) Geochemical and temporal evolution of Cenozoic magmatism in western Turkey: mantle response to collision, slab breakoff, and lithospheric tearing in an orogenic belt. Geol Soc Spec Publ 311:213–233

Duretz T, Gerya TV, May DA (2011) Numerical modelling of spontaneous slab breakoff and subsequent topographic response. Tectonophysics 502:244–256

Geng QR, Zhang Z, Peng ZM, Guang JL, Zhu XP, Mao XC (2016) Jurassic–Cretaceous granitoids and related tectono-metallogenesis in the Zapug–Duobuza arc, western Tibet. Ore Geol Rev 77:163–175

Girardeau J, Marcoux J, Allègre CJ, Bassoullet JP, Tang YK, Xiao XC, Zhao YG, Wang XB (1984) Tectonic environment and geodynamic significance of the Neo-Cimmerian Donqiao ophiolite, Bangong-Nujiang suture zone, Tibet. Nature 307:27–31

Griffin WL, Pearson NJ, Belousova E, Jackson SE, van Achterbergh E, O'Reilly SY, Shee SR (2000) The Hf isotope composition of cratonic mantle: LAM–MC–ICPMS analysis of zircon megacrysts in kimberlites. Geochim Cosmochim Acta 64:133–147

Griffin WL, Wang X, Jackson SE, Pearson NJ, O'Reilly SY, Xu XS, Zhou XM (2002) Zircon chemistry and magmamixing, SE China: in situ analysis of Hf isotopes, Tongluand Pingtan igneous complexes. Lithos 61:237–269

Guan Q, Zhu DC, Zhao ZD, Dong GC, Zhang LL, Li XW, Liu M, Mo XX, Liu YS, Yuan HL (2012) Crustal thickening prior to 38 Ma in southern Tibet: evidence from lower crust-derived adakitic magmatism in the Gangdese Batholith. Gondwana Res 21:88–99

Guynn JH, Kapp P, Pullen A, Heizler M, Gehrels G, Ding L (2006) Tibetan basement rocks near Amdo reveal "missing" Mesozoic tectonism along the Bangong suture, central Tibet. Geology 34:505–508

Hawkesworth CJ, Gallagher K, Hergt JM, McDermott F (1993) Mantle and slab contributions in ARC magmas. Annu Rev Earth Planet Sci 21:175–204

Hibbard MJ (1991) Textural anatomy of twelve magma-mixed granitoid systems. In: Didier J, Barbarin B (eds) Enclaves and granite petrology. Dev Petrol 13. Elsevier, Amsterdam, pp 431–444

Holden P, Halliday AN, Stephens WE (1987) Neodymium and strontium isotope content of microdiorite enclaves points to mantle input to granitoid production. Nature 330:53–56

Hou ZQ, Zheng YC, Yang ZM, Rui ZY, Zhao ZD, Jiang SH, Qu XM, Sun QZ (2013) Contribution of mantle components within juvenile lower-crust to collisional zoneporphyry Cu systems in Tibet. Miner Depos 48:173–192

Jahn BM, Wu FY, Hong DW (2000) Important crustal growth in the Phanerozoic: isotopice vidence of granitoids from East-Central Asia. Proc Indian Acad Sci (Earth Planet Sci Lett) 109:5–20

Kapp P, Yin A, Harrison TM, Ding L (2005) Cretaceous-tertiary shortening, basin development, and volcanism in central Tibet. Geol Soc Am Bull 117:865–878

Kapp P, DeCelles PG, Gehrels GE, Heizler M, Ding L (2007) Geological records of the Lhasa-Qiangtang and Indo-Asian collisions in the Nima area of central Tibet. Geol Soc Am Bull 119:917–932

Karsli O, Chen B, Aydin F, Sen C (2007) Geochemical and Sr–Nd–Pb isotopic compositions of the EoceneDölek and Sariçiçek Plutons, Eastern Turkey: implications for magma interaction in the genesis of high-K calc-alkaline granitoids in a post-collision extensional setting. Lithos 98:67–96

Karsli O, Dokuz A, Uysal I, Aydin F, Kandemir R, Wijbrans J (2010) Generation of the Early Cenozoic adakitic volcanism by partial melting of mafic lower crust, Eastern Turkey: implications for crustal thickening to delamination. Lithos 114:109–120

Kaygusuz A, Aydincakir K (2009) Mineralogy, whole-rock and Sr–Nd isotope geochemistry of mafic microgranular enclaves in Cretaceous Dagbasigranitoids, Eastern Pontides, NE Turkey: evidence of magma mixing, mingling and chemical equilibration. Chem Erde-Geochem 69:247–277

Kemp AIS, Hawkesworth CJ (2006) Using hafnium and oxygen isotopes in zircons to unravel the record of crustal evolution. Chem Geol 226:144–162

Kemp AIS, Hawkesworth CJ, Foster GL, Paterson BA, Woodhead JD, Hergt JM, Gray CM, Whitehouse MJ (2007) Magmatic and

crustal differentiation history of granitic rocks from Hf–O isotopes in zircon. Science 315:980–983

Lai SC, Qin JF (2008) Petrology and geochemistry of the granulite xenoliths from Cenozoic Qiangtang volcanic field: implication for the nature of the lower crust in the northern Tibetan plateau and the genesis of Cenozoic volcanic rocks. Acta Petrol Sin 24:325–336 **(in Chinese with English abstract)**

Leier AL, Decelles PG, Kapp P, Gehrels GE (2007) Lower Cretaceous strata in the Lhasa terrane, Tibet, with implications for understanding the early tectonic history of the Tibetan Plateau. J Sediment Res 77:809–825

Li CN (2002) Comment on the magma mixing and their research. Geol Sci Technol Inf 21:49–54 **(in Chinese with English abstract)**

Li XH, Li ZX, Zhou HW, Liu Y, Kinny PD (2002) U-Pb zircon geochronology, geochemistry and Nd isotopic study of Neoproterozoic bimodal volcanic rocks in the Kangdian Rift of south China: implications for the initial rifting of Rodinia. Precambrian Res 113:135–154

Li XH, Li ZX, Li WX, Liu Y, Yuan C, Wei GJ, Qi CS (2007) U-Pb zircon geochemical and Sr–Nd–Hf isotopic constraints on age and origin of Jurassic I-and A-type granites from central Guangdong, SE China: a major igneous event in response to foundering of a subducted flat-slab? Lithos 96:186–204

Li XH, Li WX, Wang XC, Li QL, Liu Y, Tang GQ (2009a) Role of mantle-derived magma in genesis of early Yanshanian granites in the Nanling Range, South China: in situ zircon Hf–O isotopic constraints. Sci China Ser D 39:872–887 **(in Chinese with English abstract)**

Li JW, Zhao XF, Zhou MF, Ma CQ, de Souza ZS, Vasconcelos P (2009b) Late Mesozoic magmatism from the Daye region, eastern China: U–Pb ages, petrogenesis, and geodynamic implications. Contrib Miner Petrol 157:383–409

Li JX, Qin KZ, Li GM, Xiao B, Zhao JX, Chen L (2011) Magmatic-hydrothermal evolution of the Cretaceous Duolong gold-rich porphyry copper deposit in the Bangongco metallogenic belt, Tibet: evidence from U-Pb and 40Ar/39Ar geochronology. J Asian Earth Sci 41:525–536

Li YL, He J, Wang CS, Santosh M, Dai JG, Zhang YX, Wei YS, Wang JG (2013a) Late Cretaceous K-rich magmatism in central Tibet: evidence for early elevation of the Tibetan plateau? Lithos 160–161:1–13

Li JX, Qin KZ, Li GM, Xiao B, Zhao JX, Cao MJ, Chen L (2013b) Petrogenesis of ore-bearing porphyries from the Duolong porphyry Cu–Au deposit, central Tibet: evidence from U–Pb geochronology, petrochemistry and Sr–Nd–Hf–O isotope characteristics. Lithos 160–161:216–227

Li JX, Qin KZ, Li GM, Richards JP, Zhao JX, Cao MJ (2014a) Geochronology, geochemistry, and zircon Hf isotopic compositions of Mesozoic intermediate–felsic intrusions in central Tibet: petrogenetic and tectonic implications. Lithos 198–199:77–91

Li SM, Zhu DC, Wang Q, Zhao ZD, Sui QL, Liu SA, Liu D, Mo XX (2014b) Northward subduction of Bangong–Nujiang Tethys: insight from Late Jurassic intrusive rocks from Bangong Tso in western Tibet. Lithos 205:284–297

Li YL, He J, Wang CS, Han ZP, Ma P, Xu M, Du KY (2015a) Cretaceous volcanic rocks in south Qiangtang Terrane: products of northward subduction of the Bangong–Nujiang Ocean? J Asian Earth Sci 104:69–83

Li YL, Wang CS, Dai JG, Xu GQ, Hou YL, Li XH (2015b) Propagation of the deformation and growth of the Tibetan–Himalayan orogen: a review. Earth Sci Rev 143:36–61

Li YL, He J, Han ZP, Wang CS, Ma PF, Zhou A, Liu SA, Xu M (2016a) Late Jurassic sodium-rich adakitic intrusive rocks in the southern Qiangtang terrane, central Tibet, and their implications for the Bangong–Nujiang Ocean subduction. Lithos 245:34–46

Li JX, Qin KZ, Li GM, Xiao B, Zhao JX, Chen L (2016b) Petrogenesis of Cretaceous igneous rocks from the Duolong porphyry Cu–Au deposit, central Tibet: evidence from zircon U–Pb geochronology, petrochemistry and Sr–Nd–Pb–Hf isotope characteristics. Geol J 51:285–307

Liu W, Li FQ, Yuan SH, Zhang WP, Zhuo JW, Wang BD, Tang WQ (2010) Volcanic rock provenance of Zenong Group in Coqen area of Tibet: geochemistry and Sr–Nd isotopic constraint. Acta Petrol Et Miner 29:367–376 **(in Chinese with English abstract)**

Liu DL, Shi RD, Ding L, Huang QS, Zhang XR, Yue YH, Zhang LY (2015) Zircon U–Pb age and Hf isotopic compositions of Mesozoic granitoids in southern Qiangtang, Tibet: implications for the subduction of the Bangong–Nujiang Tethyan Ocean. Gondwana Res, Tibet. doi:10.1016/j.gr.2015.04.007

Ma GL, Yue YH (2010) Cretaceous volcanic rocks in northern Lhasa Block: constraints on the tectonic evolution of the Gangdese Arc. Acta Petrol Et Miner 29:525–538 **(in Chinese with English abstract)**

Maniar PD, Piccoli PM (1989) Tectonic discrimination of granitoids. Geol Soc Am Bull 101:635–643

Mo XX, Hou ZQ, Niu YL, Dong GC, Qu X, Zhao ZD, Yang Z (2007) Mantle contributions to crustal thickening during continental collision: evidence from Cenozoic igneous rocks in southern Tibet. Lithos 96:225–242

Pan GT, Wang LQ, Li RS, Yuan SH, Ji WH, Yin FG, Zhang WP, Wang BD (2012) Tectonic evolution of the Qinghai-Tibet Plateau. J Asian Earth Sci 53:3–14

Pearce JA, Mei HJ (1988) Volcanic rocks of the 1985 Tibet Geotraverse: lhasa to Golmud. Philo Trans R Soc A 327:169–201

Pearce JA, Harris NBW, Tindle AG (1984) Trace element discrimination diagrams for the tectonic interpretations of granitic rocks. J Petrol 25:956–983

Peccerillo A, Taylor DR (1976) Geochemistry of Eocene calcalkaline volcanic rocks from Kastamonu area, Northern Turkey. Contrib Miner Petrol 58:63–91

Pu W, Gao JF, Zhao KD, Ling HF, Jiang SY (2005) Separation method of Rb–Sr, Sm–Nd using DCTA and HIBA. J Nanjing Univ (Nature Sciences) 41:445–450 **(in Chinese with English abstract)**

Qu XM, Xin HB (2006) Ages and tectonic environment of the Bangong Co porphyry copper belt in western Tibet, China. Geol Bull China 25(7):792–799 **(in Chinese with English abstract)**

Schneider W, Mattern F, Wang P, Li C (2003) Tectonic and sedimentary basin evolution of the eastern Bangong-Nujiang zone (Tibet): a reading cycle. Geol Rundsch 92:228–254

Silva MMVG, Neiva AMR, Whitehouse MJ (2000) Geochemistry of enclaves and host granites from the Nelasarea, central Portugal. Lithos 50:153–170

Sisson TW, Ratajeski K, Hankins WB, Glazner AF (2005) Voluminous granitic magmasfrom common basaltic sources. Contrib Miner Petrol 148:635–661

Sui QL, Wang Q, Zhu DC, Zhao ZD, Chen Y, Santosh M, Hu ZC, Yuan HL, Mo XX (2013) Compositional diversity of ca. 110 Ma magmatism in the northern Lhasa Terrane, Tibet: implications for the magmatic origin and crustal growth in a continent–continent collision zone. Lithos 168–169:144–159

Todt W, Cliff RA, Hanser A (1996) Evaluation of a ^{202}Pb–^{205}Pb double spike for high precision lead isotope analysis. Geophys Monogr Ser 95:429–437

Vernon RH (1984) Microgranitoid enclaves in granites: globules of hybrid magma quenched in a plutonic environment. Nature 309:438–443

von Blanckenburg F, Davis JH (1995) Slab breakoff: a model for syncollisional magmatism and tectonics in the Alps. Tectonics 14:120–131

Waight TE, Maas R, Nicholls IA (2000) Fingerprinting feldspar phenocrysts using crystal isotopic composition stratigraphy: implications for crystal and magma mingling in S-type granites. Contrib Miner Petrol 139:227–239

Wang XS, Hu RZ, Bi XW, Leng CB, Pan LC, Zhu JJ, Chen YW (2014) Petrogenesis of Late Cretaceous I-type granites in the southern Yidun Terrane: new constraints on the Late Mesozoic tectonic evolution of the eastern Tibetan Plateau. Lithos 208:202–219

Wen DR, Chung SL, Song B, Iizuka Y, Yang HJ, Ji J, Liu D, Gallet S (2008) Late Cretaceous Gangdese intrusions of adakitic geochemical characteristics, SE Tibet: petrogenesis and tectonic implications. Lithos 105:1–11

Wilson M (1989) Igneous petrogenesis. Unwin Hyman, London

Wong A, Ton SYM, Wortel MJR (1997) Slab detachment in continental collision zones: an analysis of controlling parameters. Geophys Res Lett 24:2095–2098

Wu FY, Jahn BM, Wilde SA, Lo CH, Yui TF, Lin Q, Ge WC, Sun DY (2003) Highly fractionated I-type granites in NE China (I): geochronology and petrogenesis. Lithos 66:241–273

Wu FY, Yang YH, Xie LW, Yang JH, Xu P (2006) Hf isotopic compositions of the standard zircons and baddeleyites used in U–Pb geochronology. Chem Geol 234:105–126

Wu FY, Li XH, Zheng YF, Gao S (2007) Lu–Hf isotopic systematics and their applications in petrology. Acta Petrol Sin 23(2):185–220 (in Chinese with English abstract)

Wyborn D, Chappell BW, James M (2001) Examples of convective fractionation in high temperature granites from the Lachlan Fold Belt. Aust J Earth Sci 48:531–541

Xin HB, Qu XM, Wang RJ, Liu HF, Zhao YY, Huang W (2009) Geochemistry and Pb, Sr, Nd isotopic features of ore-bearing porphyries in Bangong Lake porphyry copper belt, western Tibet. Miner Depos 28:785–792 (in Chinese with English abstract)

Xu RH, Scharer U, Allègre CJ (1985) Magmatism and metamorphism in the Lhasa block (Tibet): a geochronological study. J Geol 93:41–57

Yang JH, Wu FY, Chuang SL, Simon A, Chu MF (2004) Multiple sources for the origin of granites: geochemical and Nd/Sr isotopic evidence from the Gudaoling granite and its mafic enclaves, northeast China. Geochim Cosmochim Acta 68:4469–4483

Yang JH, Wu FY, Liu XM (2007) Petrogenesis and tectonic implications of Kuangdonggou syenites in the Liaodong peninsula, east North China Craton: constraints from In-situ zircon U–Pb ages and Hf isotopes. Acta Petrol Sin 23:263–276 (in Chinese with English abstract)

Yin A, Harrison TM (2000) Geologic evolution of the Himalayan-Tibetan orogen. Annu Rev Earth Planet Sci 28:211–280

Zhang YX (2007) Tectonic evolution of the middle-western Bangong–Nujiang suture, Tibet. Dissertation, Chinese academy of sciences (in Chinese with English abstract)

Zhang KJ, Tang XC (2009) Eclogites in the interior of the Tibetan plateau and their geodynamic implications. Chin Sci Bull 54:2556–2567

Zhang KJ, Xia BD, Wang GM, Li YT, Ye HF (2004) Early Cretaceous stratigraphy, depositional environments, sandstone provenance, and tectonic setting of central Tibet, western China. Geol Soc Am Bull 116:1202–1222

Zhang ZC, Dong SY, Huang H, Ma LT, Zhang DY, Zhang S, Xue CJ (2009) Geology and geochemistry of the Permian intermediate-acid intrusions in the southwestern Tianshan, Xinjiang, China: implications for petrogenesis and tectonics. Geol Bull China 28:27–1839 (in Chinese with English abstract)

Zhang LL, Zhu DC, Zhao ZD, Dong GC, Mo XX, Guan Q, Liu M, Liu MH (2010) Petrogenesis of magmatism in the baerda region of Northern Gangdese, Tibet: constraints from geochemistry, geochronology and Sr–Nd–Hf isotopes. Acta Petrol Sin 26:1871–1888 (in Chinese with English abstract)

Zhang LL, Zhu DC, Zhao ZD, Liao ZL, Wang LQ, Mo XX (2011) Early cretaceous granitoids in Xainza, Tibet: eVidence of slab break-off. Acta Petrol Sin 27:1938–1948 (in Chinese with English abstract)

Zhang KJ, Zhang YX, Tang XC, Xia B (2012a) Late Mesozoic tectonic evolution and growth of the Tibetan plateau prior to the Indo-Asian collision. Earth Sci Rev 114:236–249

Zhang XQ, Zhu DC, Zhao ZD, Sui QL, Wang Q, Yuan SH, Hu ZC, Mo XX (2012b) Geochemistry, zircon U–Pb geochronology and in situ Hf isotope of the Maiga batholith in Coqen, Tibet: constraints on the petrogenesis of the Early Cretaceous granitoids in the central Lhasa Terrane. Acta Petrol Sin 28:1615–1634 (in Chinese with English abstract)

Zhao ZD, Mo XX, Dilek Y, Niu YL, DePaolo DJ, Robinson P, Zhu DC, Sun CG, Dong GC, Zhou S, Luo ZH, Hou ZQ (2009) Geochemical and Sr–Nd–Pb–O isotopic compositions of the post-collisional ultrapotassic magmatism in SW Tibet: petrogenesis and implications for India intro-continental subduction beneath southern Tibet. Lithos 113:190–212

Zhu DC, Pan GT, Mo XX, Wang LQ, Liao ZL, Zhao ZD, Dong GC, Zhou CY (2006a) Late jurassic-early cretaceous geodynamic setting in middle-northern Gangdese: new insights from volcanic rocks. Acta Petrol Sin 22:534–546 (in Chinese with English abstract)

Zhu DC, Pan GT, Mo XX, Wang LQ, Zhao ZD, Liao ZL (2006b) Identification of the Mesozoic OIB-type basalts in central Qinghai-Tibetan Plateau: geochronology, geochemistry and their tectonic setting. Acta Geol Sin 80:1312–1328 (in Chinese with English abstract)

Zhu DC, Mo XX, Niu YL, Zhao ZD, Wang LQ, Liu YS, Wu FY (2009a) Geochemical investigation of early cretaceous igneous rocks along an east-west traverse throughout the central Lhasa Terrane, Tibet. Chem Geol 268:298–312

Zhu DC, Mo XX, Wang LQ, Zhao ZD, Niu YL, Zhou CY, Yang YH (2009b) Petrogenesis of highly fractionated I-type granites in the Zayu area of eastern Gangdese, Tibet: constraints from zircon U–Pb geochronology, geochemistry and Sr–Nd–Hf isotopes. Sci China Ser D 52:1223–1239

Zhu DC, Zhao ZD, Pan GT, Lee HY, Kang ZQ, Liao ZL, Wang LQ, Li GM, Dong GC, Liu B (2009c) Early cretaceous subduction-related adakite-like rocks of the Gangdese Belt, southern Tibet: products of slab melting and subsequent melt-peridotite interaction? J Asian Earth Sci 34:298–309

Zhu DC, Zhao ZD, Niu YL, Mo XX, Chung SL, Hou ZQ, Wang LQ, Wu FY (2011) The Lhasa Terrane: record of a microcontinent and its histories of drift and growth. Earth Planet Sci Lett 301:241–255

Zhu DC, Zhao ZD, Niu YL, Dilek Y, Hou ZQ, Mo XX (2013) The origin and pre-Cenozoic evolution of the Tibetan Plateau. Gondwana Res 23:1429–1454

Zhu DC, Li SM, Cawood PA, Wang Q, Zhao ZD, Liu SA, Wang LQ (2016) Assembly of the Lhasa and Qiangtang terranes in central Tibet by divergent double subduction. Lithos 245:7–17

Zorpi MJ, Coulon C, Orisini JB (1991) Hybridization between felsic and mafic magma in calk-alkaline granitoids: a case study in northern Sardinia, Italy. Chem Geol 92:45–86